

Rapid patient-specific neural networks for intraoperative X-ray to volume registration

Vivek Gopalakrishnan^{†1,2,3}, Neel Dey², David-Dimitris Chlorogiannis³, Andrew Abumoussa⁴, Anna M. Larson⁵, Darren B. Orbach⁵, Sarah Frisken³, and Polina Golland^{†1,2}

¹Harvard-MIT Health Sciences and Technology, Massachusetts Institute of Technology, Cambridge, MA, USA

²Computer Science and Artificial Intelligence Laboratory, Massachusetts Institute of Technology, Cambridge, MA, USA

³Department of Radiology, Brigham and Women's Hospital and Harvard Medical School, Boston, MA, USA

⁴Department of Neurosurgery, University of North Carolina School of Medicine, Chapel Hill, NC, USA

⁵Department of Interventional Neuroradiology, Boston Children's Hospital, Boston, MA, USA

[†]Correspondence to: {vivekg, polina}@csail.mit.edu

Abstract. The integration of artificial intelligence in image-guided interventions holds transformative potential, promising to extract 3D geometric and quantitative information from conventional 2D imaging modalities during complex procedures. Achieving this requires the rapid and precise alignment of 2D intraoperative images (e.g., X-ray) with 3D preoperative volumes (e.g., CT, MRI). However, current 2D/3D registration methods fail across the broad spectrum of procedures dependent on X-ray guidance: traditional optimization techniques require custom parameter tuning for each subject, whereas neural networks trained on small datasets do not generalize to new patients or require labor-intensive manual annotations, increasing clinical burden and precluding application to new anatomical targets. To address these challenges, we present *xvr*, a fully automated framework for training *patient-specific* neural networks for 2D/3D registration. *xvr* uses physics-based simulation to generate abundant high-quality training data from a patient's own preoperative volumetric imaging, thereby overcoming the inherently limited ability of supervised models to generalize to new patients and procedures. Furthermore, *xvr* requires only 5 min of training per patient, making it suitable for emergency interventions as well as planned procedures. We perform the largest evaluation of a 2D/3D registration algorithm on real X-ray data to date and find that *xvr* robustly generalizes across a diverse dataset comprising multiple anatomical structures, imaging modalities, and hospitals. Across surgical tasks, *xvr* achieves submillimeter-accurate registration at intraoperative speeds, improving upon existing methods by an order of magnitude. *xvr* is released as open-source software freely available at <https://github.com/eigenvivek/xvr>.

1 Introduction

Each year, millions of clinical interventions are performed using real-time X-ray image guidance (*i.e.*, fluoroscopy) [1]. The extensive application of intraoperative fluoroscopy across specialties—including neurosurgery [2, 3], orthopedics [4, 5], endovascular surgery [6, 7], radiation oncology [8–10], and interventional radiology [11–14]—has significantly improved patient outcomes by minimizing invasiveness, shortening postoperative recovery times, and expanding access to life-saving treatments for patients considered too high risk for open surgery [15, 16].

Acquired using highly maneuverable C-arm imaging devices, real-time fluoroscopy enables the noninvasive visualization of an intervention from virtually any angle. However, the projectional nature of X-ray imaging introduces an inherent geometric deficiency: two-dimensional (2D) X-rays do not provide explicit depth information, unlike the direct anatomical visualization afforded by open surgery. This spatial ambiguity encumbers the navigation of medical devices within three-dimensional (3D) anatomical structures, increasing the risks of suboptimal device deployment and intraoperative complications [17]. For example, due to the difficulty in differentiating individual vertebrae on X-ray, nearly 50% of spinal neurosurgeons have reported operating on the wrong vertebra at least once in their careers [18, 19]. As a result, image-based navigation is complicated by the cognitive burden of implicitly reconstructing 3D anatomy from intraoperative 2D X-ray projections in real time.

In contrast, volumetric imaging modalities, such as computed tomography (CT), positron emission tomography (PET), and magnetic resonance imaging (MRI), offer high-

resolution 3D anatomical and functional visualization [20]. While these 3D modalities are routinely acquired preoperatively, they are often unavailable during procedures due to their high radiation dose or incompatibility with surgical equipment and workflows [21]. Furthermore, 3D imaging has lengthy acquisition and reconstruction times, which diminishes its utility in real-time surgical navigation. Consequently, live 3D spatial information is inaccessible during most interventions, and mono- or biplane C-arm fluoroscopy remains the intraoperative standard for image guidance.

As a promising alternative, volumetric image guidance can be emulated by rapidly registering the 2D fluoroscopic images acquired intraoperatively with 3D preoperative scans, enabling the localization of medical devices relative to 3D patient anatomy. This capability makes 2D/3D registration critical to the development of numerous advanced image-based navigation techniques with artificial intelligence, such as vertebral level localization in spinal neurosurgery [22], reprojection of patient-specific preoperative plans onto intraoperative images [23–25], 4D tracking of surgical instruments using epipolar geometry [26, 27], motion correction of 3D radiotherapy plans in radiation oncology [28, 29], pose estimation for intraoperative cone-beam CT reconstruction in bronchoscopy-guided biopsies [30], and the establishment of global coordinate frames for surgical robotics systems [31].

Despite its broad potential utility, achieving reliable, accurate, and automated 2D/3D registration across these diverse clinical practices remains a challenge [32]. Conventional registration methods typically combine iterative optimization with computational imaging models, searching for the position and orientation (*i.e.*, pose) of the C-arm that generates

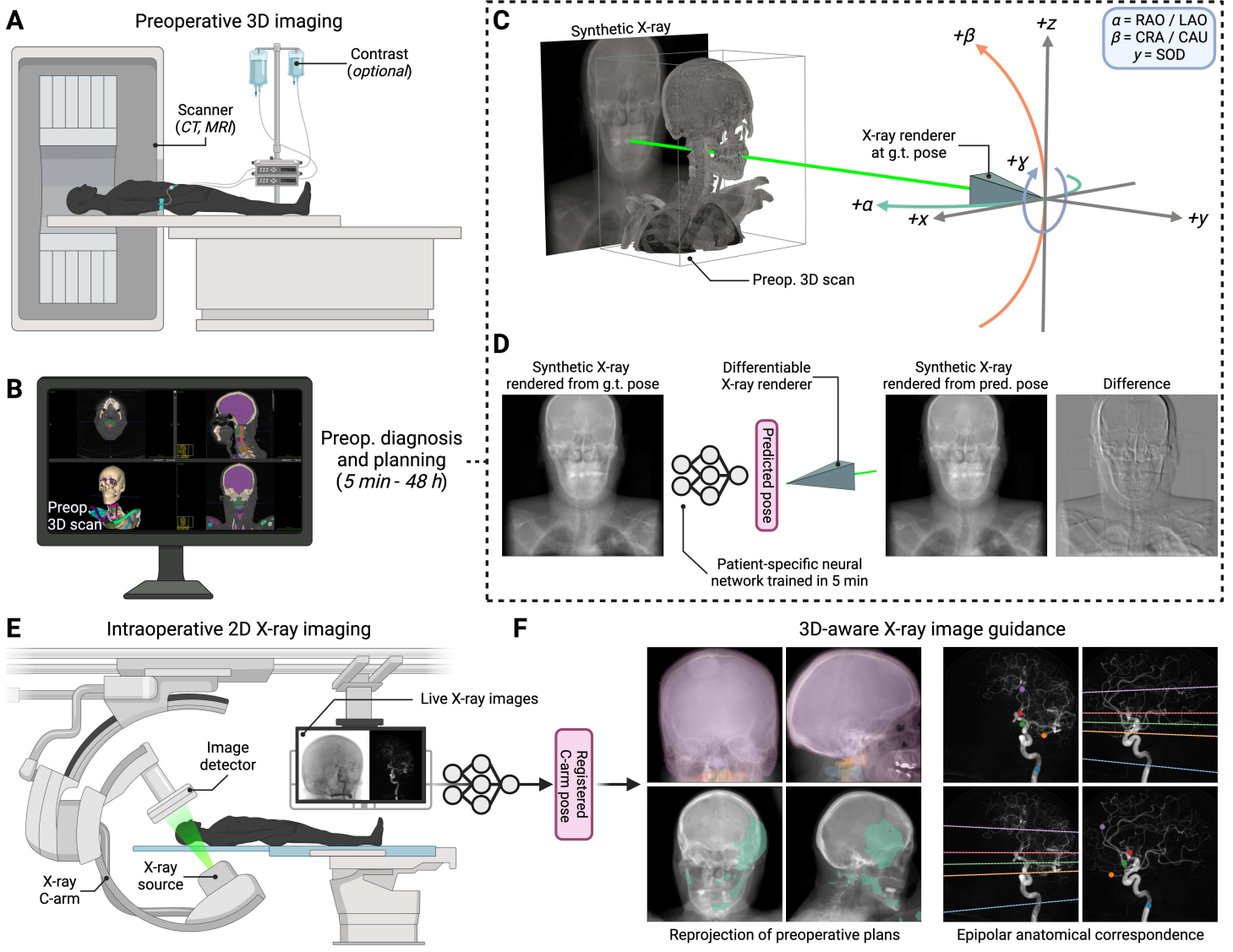


Figure 1. Rapidly trained patient-specific neural networks with xvr achieve submillimeter accuracy in intraoperative 2D/3D registration without disrupting existing clinical workflows. (A) Preoperative 3D imaging (e.g., CT or MRI) is commonly acquired before many image-guided procedures. (B) Clinical teams make diagnoses and preoperative plans from these scans, which can take anywhere from minutes to multiple days depending on the intervention (e.g., stroke vs. radiotherapy). (C and D) During the preoperative phase, we train a patient-specific network to regress the ground truth (g.t.) pose of a synthetic training X-ray rendered from the patient's 3D imaging. These synthetic X-rays are generated using our differentiable X-ray renderer, which is designed to simulate the imaging physics and geometry of a C-arm. With xvr, patient-specific neural networks can be trained in as little as 5 min. (E) Intraoperatively, 3D volumes can no longer be acquired, and live 2D X-rays are used instead for guidance. (F) Trained networks are then deployed during interventions, performing accurate 2D/3D registration in seconds. This enables numerous applications for 3D-aware image guidance, such as the reprojection of 3D preoperative plans onto intraoperative imaging to highlight interventional targets or the identification of shared anatomical structures across multiple X-ray images of the patient using epipolar geometry.

a synthetic X-ray from the preoperative 3D volume that most closely matches the real X-ray [33–38]. While iterative optimization with synthetic X-rays (referred to as digitally reconstructed radiographs in the medical imaging literature) can yield accurate registration results, it is highly sensitive to errors in the initial pose estimate: if an iterative solver is initialized even a few centimeters from the true C-arm pose, it can fail to converge to the correct solution [39–43], leading to significant intraoperative consequences [44].

To this end, numerous deep learning-based approaches have been proposed to produce better initial pose estimates,

either by identifying shared anatomical landmarks in the 2D and 3D images [45–49] or by directly regressing the pose of the C-arm from a 2D X-ray [50–53]. However, supervised landmark-based methods require expert knowledge of structures that are reliably visible in X-ray, as well as manual annotation of these 3D landmarks for every new preoperative scan, constraining such models to the particular anatomy for which they were trained [54]. Moreover, surgical patients frequently present with non-standard anatomy such as fractures, implanted medical devices, cancerous growths, or musculoskeletal degeneration and deformities. This hetero-

geneity challenges the development of both pose regression and landmark-based registration methods: there exist limited quantities of labeled training data, increasing the likelihood that a model trained in a purely supervised fashion will fail to generalize to new patients encountered in real clinical settings [55]. Furthermore, the immense effort required on the part of clinicians to manually label these small datasets renders existing supervised deep learning approaches insufficient to provide a precise and scalable solution for generic 2D/3D registration.

To address the need for intraoperative 2D/3D registration, we introduce *xvr*, an automatic framework for *patient-specific* X-ray to volume registration. *xvr* enables reliable and accurate 2D/3D registration for any patient, procedure, or pathology with a two-stage protocol (Fig. 1). Preoperatively, a patient-specific neural network is trained to regress the pose of the C-arm from synthetic 2D X-ray images. These images are rendered at random from the patient’s own routinely acquired preoperative 3D volume using a computational model of X-ray image formation. Intraoperatively, this neural network initiates a multiscale iterative optimizer that refines the proposed pose via differentiable X-ray rendering in seconds, enabling submillimeter levels of registration accuracy. Unlike previous methods that rely on manually labeled data from multiple patients, *xvr* is self-supervised, leveraging patient-specific simulation to automatically generate an unlimited set of synthetic X-rays with ground truth C-arm poses on the fly.

xvr is a complete overhaul of our preliminary workshop and conference papers on differentiable X-ray rendering and 2D/3D registration [38, 53]. For life-threatening emergencies that cannot afford to train a pose regression network from scratch, we now introduce an amortized patient-agnostic pretraining strategy that reduces the time required to train a patient-specific model from hours in our previous work [53] to only five minutes. We further include a simple interface that enables practitioners to easily train their own patient-specific models and multiple new experiments to make this the largest evaluation of a 2D/3D registration method to date.

We show that our fast, personalized machine learning approach has several benefits. First, *xvr* outperforms previous supervised deep learning and unsupervised iterative optimization approaches by an order of magnitude, achieving submillimeter registration accuracy across multiple interventional specialties. Second, using rapid patient-specific finetuning, *xvr* mitigates the out-of-distribution failures of previous approaches, which occur when a new patient is not well represented by the training set. These advantages enable *xvr* to maximize its performance for the specific patient undergoing an intervention. We demonstrate the precision, speed, and breadth of clinical utility of *xvr* by analyzing two public benchmark datasets with calibrated C-arm poses and one private clinical dataset with highly heterogeneous imaging data. In total, these datasets comprise 66 unique patients across three hospitals with multiple anatomical registration structures. Finally, *xvr* is open-source software, freely released with the goal of eliminating the 2D/3D registration bottleneck in the advancement of intraoperative image guidance.

2 Results

Synthesizing patient-specific training data with differentiable X-ray rendering (Fig. 2). Machine learning models for medical imaging problems are frequently hampered by the paucity of expert-labeled data available to train accurate and generalizable models [57]. These data limitations are even more acute in interventional applications than in diagnostics, as intraoperative X-rays are frequently not saved in the electronic medical record [58, 59], and almost never with corresponding C-arm poses that could be used to train supervised models. We address this data bottleneck by generating synthetic training images from a patient’s own preoperative imaging via differentiable X-ray rendering.

To accomplish this, we developed a computational model of the physics underlying X-ray image formation (Fig. 2). Given a preoperative 3D CT or MRI scan (Fig. 2A), *xvr* uses differentiable implementations of ray tracing algorithms to render a synthetic X-ray image from a specified C-arm pose (Fig. 2B). Optionally, given a 3D label map of the input scan (Fig. 2C), *xvr* can also render specific anatomical structures, enabling the registration of individual organs or bones (Fig. 2D). Finally, the geometric parameterization of poses in *xvr* is designed to comport with the radiologic nomenclature adopted by commercial C-arms (Fig. 1C). For example, the rotational parameters α and β correspond to the left-right anterior oblique axis (LAO/RAO) and the crano-caudal axis (CRA/CAU), respectively, and the translational parameter y corresponds to the source-to-isocenter distance (SID), *i.e.*, depth. Adopting this radiologic convention makes it easier for clinical practitioners to specify ranges for the C-arm’s pose that are appropriate for a particular procedure when training patient-specific networks with *xvr*. A complete derivation of the C-arm geometry and physics implemented in *xvr* is provided in the Methods M.1 and our patient-specific training simulation is illustrated in Figure S1.

Synthetic X-rays rendered by *xvr* (Fig. 2F) are consistent with real X-ray images (Fig. 2E). Differences in appearance are mainly due to geometric deviations between the preoperative and intraoperative imaging. For example, in the pelvic illustrations, the subject’s femur moves between the two acquisitions in the second columns of Figure 2E and F. Similarly, in the neurovascular setting, the signal-to-noise ratio of 3D rotational angiography is too low to capture the smallest cranial blood vessels. As such, they do not appear in *xvr*’s renderings (Fig. 2F, center), but are visible in the real X-rays (Fig. 2E, center). Nevertheless, the position and orientation of major anatomical structures (*i.e.*, pelvis, vascular trunk, and skull) are conserved between the real and synthetic X-rays and can be used to guide 2D/3D registration. Furthermore, our renderer is fast and highly optimized, capable of rendering tens of thousands of synthetic X-ray images per minute for patient-specific training (as compared to the tens to hundreds of real X-ray images typically available when training supervised deep learning models). The fidelity and efficiency of our renderer led us to hypothesize that neural networks trained with its renderings would successfully generalize to real X-rays.

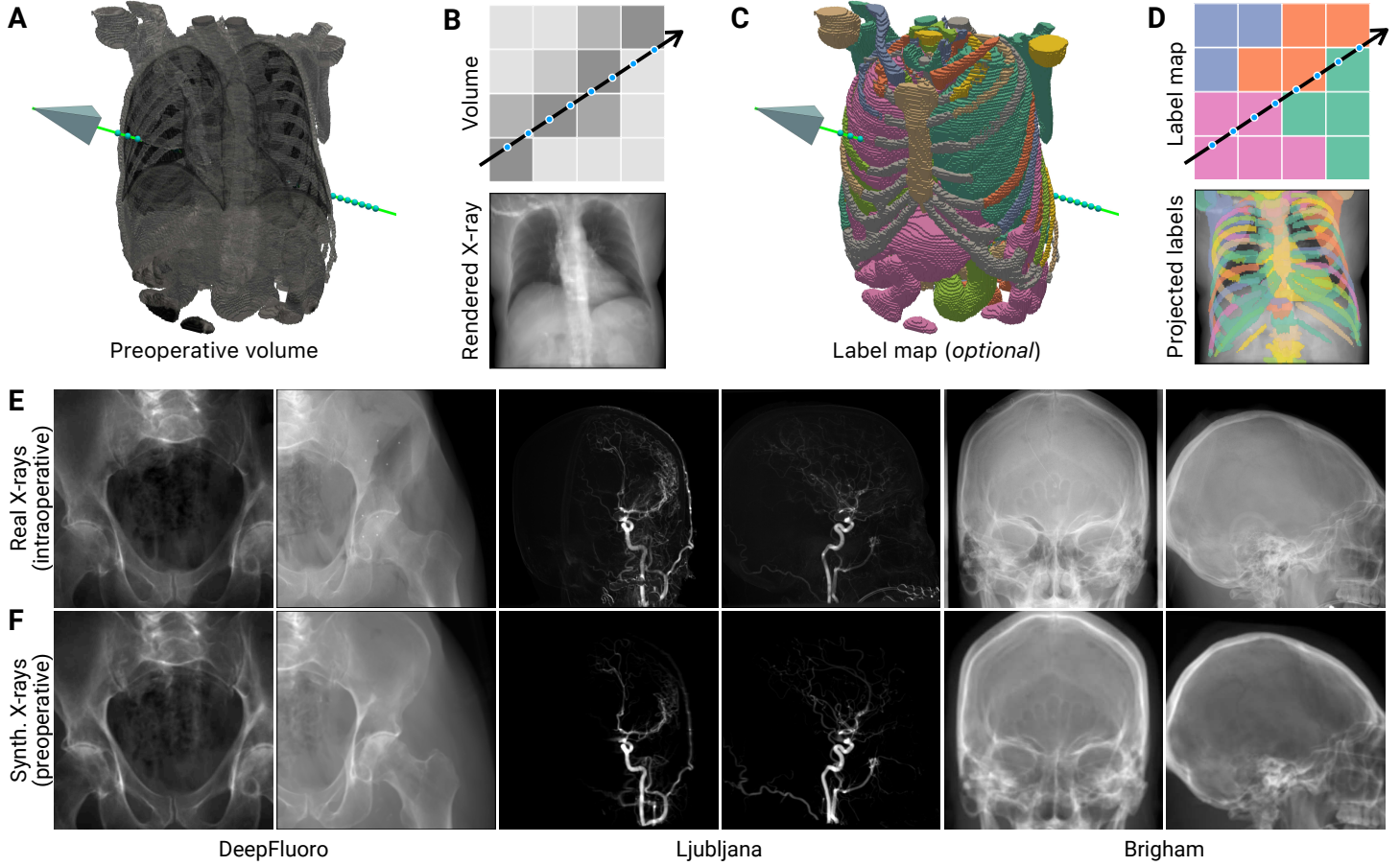
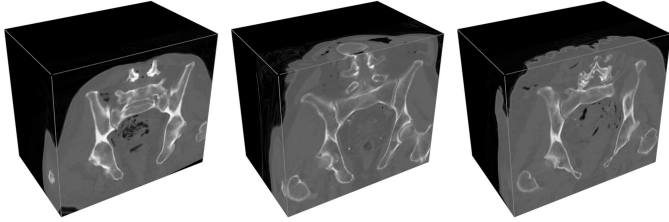


Figure 2. *xvr* implements a physics-based differentiable renderer that simulates the geometry of an X-ray C-arm to generate photorealistic X-ray images from 3D volumes. (A) Our renderer requires two inputs: a 3D volume from which to generate synthetic X-rays and the pose of the C-arm (represented with a camera frustum). Our renderer is differentiable with respect to the C-arm pose, allowing us to use gradient-based optimization to register X-ray images to 3D volumes. (B) A pictorial overview of trilinear interpolation, one of the ray tracing methods we implement to render synthetic X-rays (along with Siddon’s method [56]). (C) Optionally, a 3D label map of the preoperative volume can also be used to render X-rays of specific anatomical structures. (D) In addition to developing fully differentiable implementations of ray tracing with trilinear interpolation and Siddon’s method, we also adapt these algorithms to project 3D anatomical labels into 2D space, enabling structure-specific registration. (E and F) Comparisons of real X-rays to synthetic images rendered from volumetric imaging of the same patients using successfully registered C-arm poses demonstrate the fidelity achievable with *xvr*.

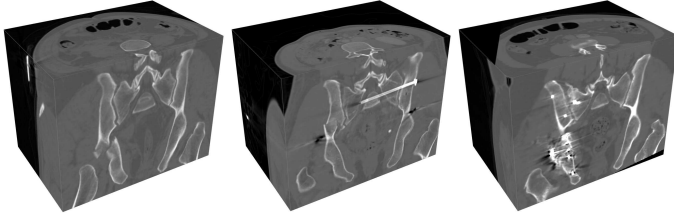
Learning to register intraoperative images in minutes via preoperative simulation (Fig. 3). To evaluate the generalization capability of neural networks trained exclusively with synthetic X-rays, we used two benchmark 2D/3D registration datasets with ground truth C-arm poses. First, we evaluated *xvr* using the DeepFluoro dataset [54], a collection of pelvic X-rays and CTs from lower body cadavers. Each subject has a CT scan and between 24 and 111 X-rays, totaling six CTs (Fig. 3A, *top*) and 366 X-rays (Fig. 2E, *left*). To measure *xvr*’s performance on images from real clinical interventions, we also used the Ljubljana dataset [60] to register 2D and 3D digital subtraction angiography (DSA) images from 10 endovascular neurosurgery patients. In this dataset, each patient has one 3D rotational DSA (rDSA) (Fig. 3B, *top*) and two 2D DSAs (Fig. 2E, *center*) as intraoperative images in endovascular procedures are commonly acquired using a biplane C-arm. Finally, numerous metrics exist to evaluate the error of a pose estimate relative to the ground truth, which we survey in the Methods M.2. We report mean Target Registration Error (mTRE) as it is the most stringent metric (Tab. S1).

We trained a *patient-specific* neural network for each subject in these two datasets using synthetic X-rays derived from their preoperative scans. The parameter ranges used for sampling synthetic C-arm poses when training networks with *xvr* are provided in Table S2. The blue curves in Figure 3 report the networks’ test accuracy, measuring their pose estimation error on real intraoperative X-rays throughout the 12 h training schedule, averaged over all subjects. Our models successfully generalized to real X-ray images, achieving a median initial pose estimation error of 31.7 mm (IQR: 18.8 mm to 45.6 mm) on DeepFluoro (Fig. 3C) and 25.0 mm (IQR: 19.8 mm to 31.4 mm) on Ljubljana (Fig. 3D). As we show later in this section, these initial pose estimates were sufficiently accurate to achieve submillimeter registration error following pose refinement via fast iterative optimization. This demonstrates that the domain shift between synthetic X-rays generated by our renderer and real X-rays acquired during interventions is insignificant for this task, and that neural networks trained exclusively on subject-specific synthetic X-rays are surgically viable.

A DeepFluoro (N=6 CTs from lower-body cadavers)



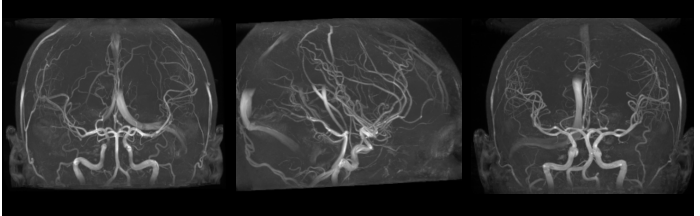
CTPelvic1K (N=178 CTs from hospitalized patients)



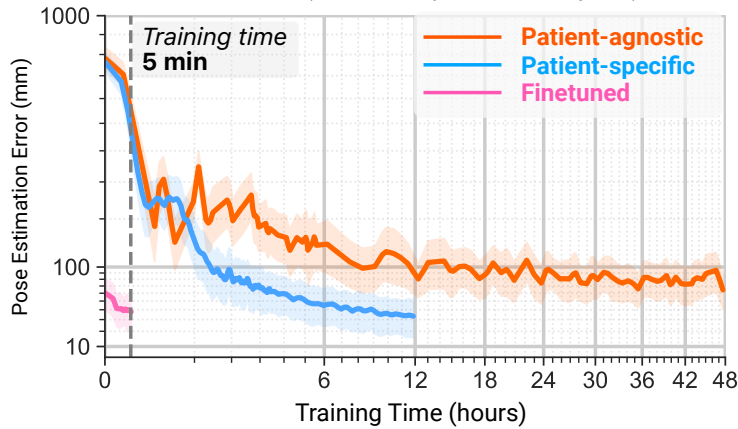
B Ljubljana (N=10 rDSAs from endovascular surgery patients)



NITRC (N=61 TOF MRAs from research study subjects)



C DeepFluoro (N=366 X-rays from 6 subjects)



D Ljubljana (N=20 X-rays from 10 patients)

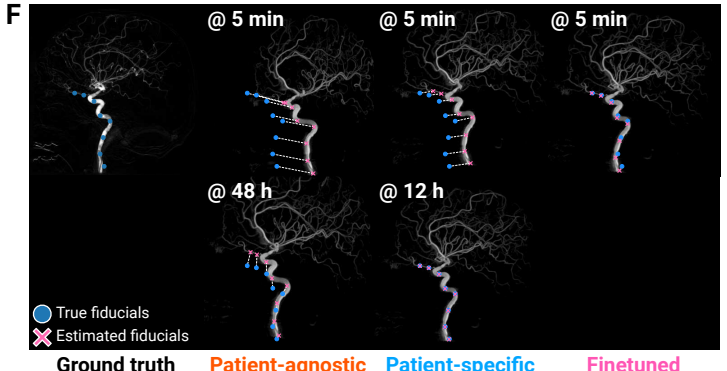
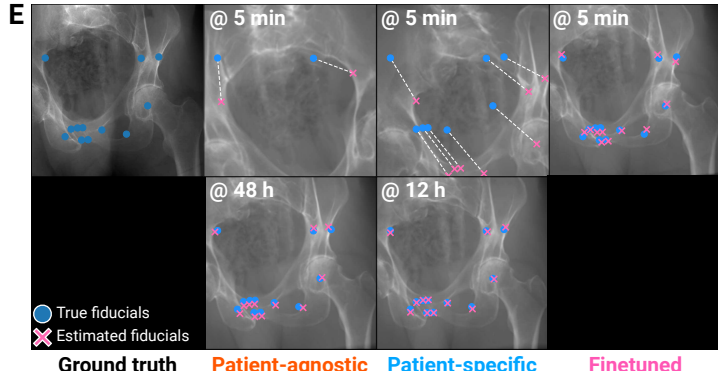
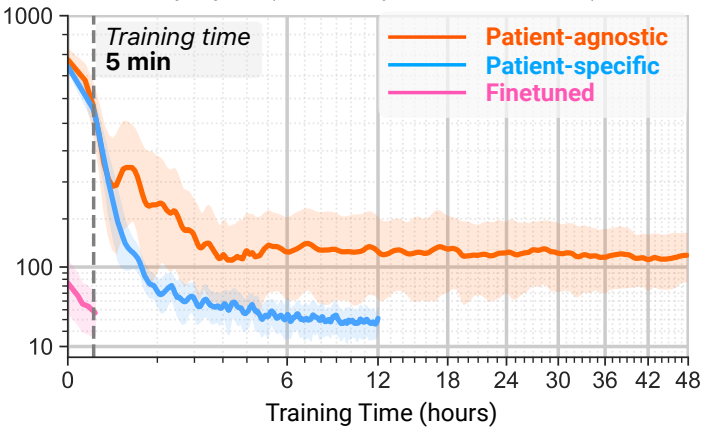


Figure 3. Pretraining on publicly available datasets enables minutes-long patient-specific finetuning. (A) 3D renderings of pelvic CT scans from lower body cadavers in the DeepFluoro dataset (top). Volumes in the CTPelvic1K dataset are clinical scans of diverse hospitalized patients and contain findings not present in DeepFluoro, such as fractures and metal implants (bottom). (B) Maximum intensity projections (MIPs) of 3D rotational DSAs (rDSAs) from the Ljubljana dataset (top). Compared to MIPs of the TOF MRAs in the NITRC dataset, rDSAs typically capture a single hemisphere of circulation and do not contain any non-vessel anatomy (bottom). (C and D) After 12 h of training on our synthetic X-ray task, patient-specific networks (blue) produce very accurate initial pose estimates (20 mm to 40 mm), while patient-agnostic networks trained for 48 h (orange) have higher error (50 mm to 80 mm for DeepFluoro and 90 mm to 190 mm for Ljubljana). A finetuned model (pink) initialized from the patient-agnostic model matches the accuracy of the patient-specific model with only 5 min of training. Error bars represent one standard deviation of pose estimation error averaged across the X-rays from all patients. (E and F) Renderings of synthetic X-rays from the pose predicted by the various models after 5 min of neural network training (top). Only the finetuned model (pink) achieves acceptable error at this stage. The patient-agnostic (orange) and patient-specific (blue) models achieve comparable accuracy after 48 h and 12 h of training, respectively (bottom). Additionally, the effects of rigid registration over center-alignment when aligning the patient-specific volume to the pretraining dataset can be noted by comparing the patient-agnostic initial pose estimates at 48 h between the DeepFluoro and Ljubljana examples. Note that ground truth and estimated fiducials are not used during pose estimation, but rather are used *post hoc* to visualize and quantify registration error.

Training a pose regression neural network *de novo* for every new patient produces highly accurate initial pose estimates, addressing the pressing intraoperative need for precise and consistent 2D/3D registration. However, this protocol is too slow for emergency interventions that cannot afford hours of preoperative training (e.g., endovascular thrombectomy for acute ischemic stroke). To overcome this limitation, we propose to first train a *patient-agnostic* base neural network using synthetic X-rays generated from a corpus of mutually preregistered scans. As this patient-agnostic model is not used directly in any intervention, it can be trained offline without time constraints. Then, given preoperative imaging for a new patient, we rapidly finetune a patient-specific model with a few iterations of our preoperative training simulation, using the patient-agnostic model weights as initialization. Our patient-specific simulation task and neural network architecture are detailed in the Methods M.3.

To train a patient-agnostic model for pelvic registration, we adapted the CTPelvic1K dataset [61], a collection of 178 clinical pelvic CTs (Fig. 3A, *bottom*). Unlike the lower body cadavers imaged in DeepFluoro (Fig. 3A, *top*), scans in CTPelvic1K are from hospitalized patients and thus contain clinical findings, such as fractures and metal implants. Scans from this dataset were first preregistered to a shared template using Advanced Normalization Tools (ANTs) [62], then used to render synthetic X-rays for 48 h of patient-agnostic training. The orange curve in Fig. 3C reports the pose estimation error of the patient-agnostic model over the course of its 48 h training schedule. Despite exclusively training on synthetic X-rays rendered from patients in CTPelvic1K, the patient-agnostic model performed well on real X-rays from subjects in DeepFluoro, achieving a median initial pose estimation error of 67.4 mm (IQR: 53.3 mm to 81.4 mm). As expected, this *patient-agnostic* error was higher than that of the six *patient-specific* models on average (Fig. 3C). However, we can rapidly improve performance by finetuning this patient-agnostic model on a new patient with transfer learning.

By initializing a network with the pretrained weights from the patient-agnostic model (instead of randomly initializing network weights as is done in *de novo* training), finetuning enables population-level features learned from the pretraining dataset to be rapidly adapted to a new patient's anatomy. Finetuning our patient-agnostic model for only 5 min on each patient in DeepFluoro produced highly accurate models that achieved an aggregate registration error of 37.1 mm (IQR: 26.3 mm to 51.3 mm) as reported in the pink curve in Fig. 3C. This shows that, by training on multiple scans comprising diverse morphologies and pathologies, patient-agnostic models build a 3D geometric understanding of anatomy that transfers to new patients. Thus, when there are sufficient data available to pretrain a patient-agnostic model, patient-specific finetuning is significantly faster than *de novo* patient-specific training. However, the ability to train a patient-specific network from scratch with *xvr* remains important for specialized scenarios, such as for patients with highly distinct anatomies (e.g., *situs inversus*). Finally, finetuning via transfer learning requires a simple coordinate transform from the pretraining dataset to the new patient (detailed in the Methods M.4).

To demonstrate *xvr*'s robustness and flexibility across diverse anatomical structures, we extended our training protocol to cases from endovascular neurosurgery. The Ljubljana dataset, collected during real clinical interventions, presents significant challenges not encountered in the DeepFluoro dataset. First, interventionalists routinely modify image acquisition parameters during procedures to enhance visualization of anatomical structures (e.g., independently panning the C-arm detector or narrowing the field of view). Unlike the controlled environment of the DeepFluoro cadaver study, each X-ray in the Ljubljana dataset features unique intrinsic parameters. This is incongruous with our network architecture (as well as other existing deep learning methods), which assumes synthetic X-rays are rendered with consistent intrinsics. To integrate into existing clinical workflows, we develop a geometric transform that resamples acquired X-rays to match the intrinsic parameters used during training, allowing the same pretrained network to be used even as the interventionalist changes acquisition parameters (Fig. S2). Second, the relative infrequency of neurovascular interventions compared to orthopedic pelvic fracture surgeries has resulted in a deficit of large, publicly available rDSA datasets for the neurovasculature, limiting our ability to pretrain patient-agnostic models. To overcome this, we used the NeurolImaging Tools & Resources Collaboratory Magnetic Resonance Angiography (NITRC MRA) Atlas [63], an open-access collection of high-resolution time-of-flight MRAs from 61 healthy subjects. These MRAs were mutually preregistered using ANTs and subsequently processed with VesselBoost [64] to extract the neurovascular tree (Fig. 3B, *bottom*).

Despite these large domain shifts, a pretrained patient-agnostic network performed well on real 2D DSA images, achieving a median pose estimation error of 130.7 mm (IQR: 89.4 mm to 190.3 mm) (Fig. 3D). This demonstrates that the modality of the pretraining dataset does not need to match that of the clinically acquired scans to produce a useful patient-agnostic network. Furthermore, we again find that finetuning patient-specific models from this initialization for 5 min produces highly accurate networks that achieve the same precision as the 12 h patient-specific training (Fig. 3D). In fact, in the first epoch of finetuning, the average error reduces from 130 mm to 60 mm, meaning the finetuned model rapidly learns to overcome any misalignment between the patient-specific preoperative imaging and the 3D pretraining dataset. These results demonstrate that our patient-agnostic pretraining simulation is highly flexible and robust to many data- and domain-specific challenges.

In Figure 3E and F, we visualize the initial C-arm poses estimated by our patient-agnostic, patient-specific, and finetuned models on sample X-rays from the DeepFluoro and Ljubljana datasets, respectively. Given only 5 min of training, the patient-agnostic and patient-specific models produce largely inaccurate pose estimates; however, the finetuned model's estimates are nearly perfect. In comparison, patient-agnostic and patient-specific models require 48 h and 12 h of training, respectively, to achieve comparable registration precision. This marked decrease in training time means that it is feasible to use *xvr* in time-sensitive procedures.

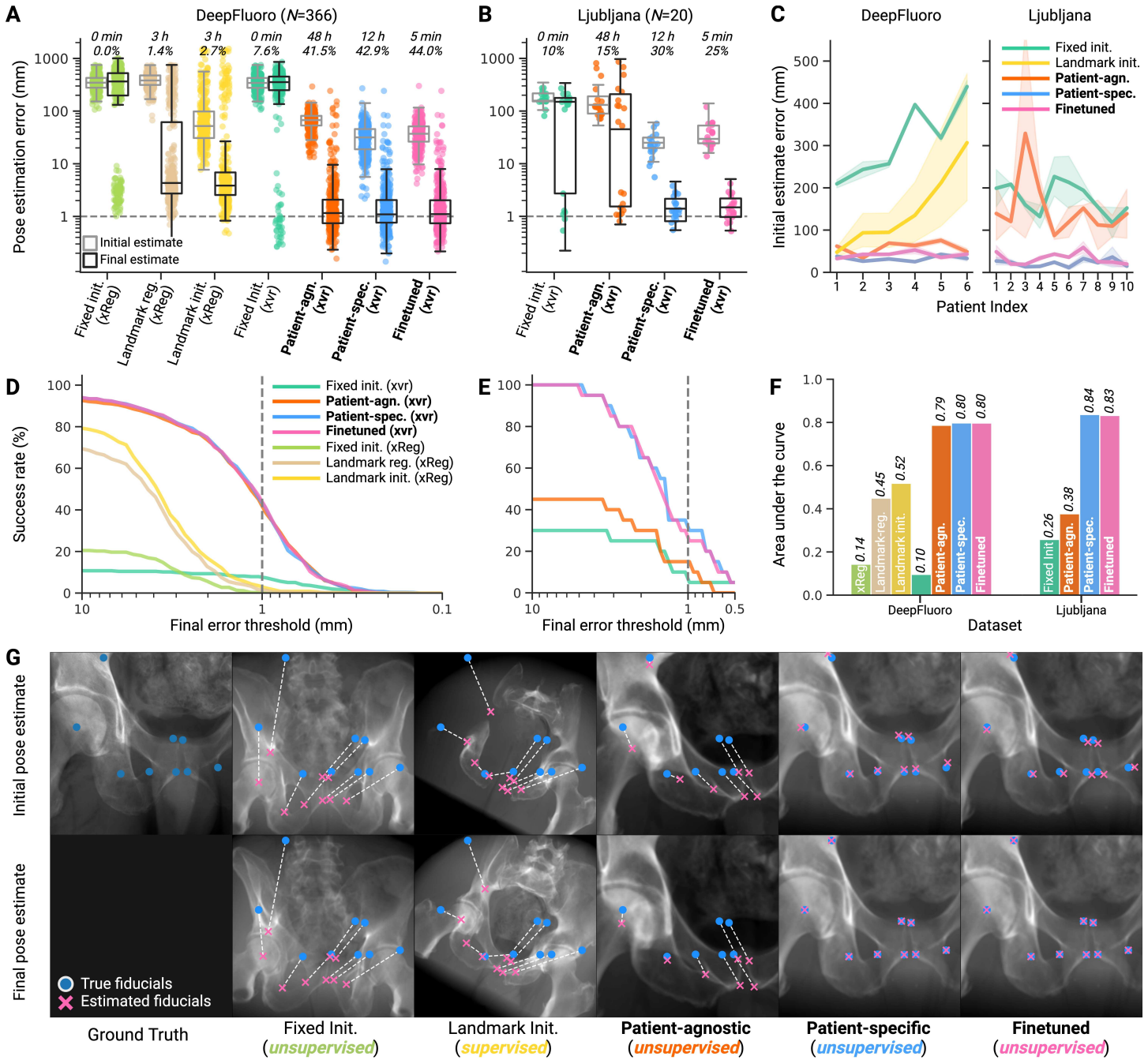


Figure 4. Differentiable pose refinement achieves submillimeter registration accuracy. (A and B) Initial and final pose estimate errors for multiple initialization and iterative pose refinement strategies. Each method is annotated with the amount of neural network training time required, the percentage of X-rays that are successfully registered with less than 1 mm of error, and the renderer used to drive pose refinement. The bolded methods (**patient-agnostic**, **patient-specific**, and **finetuned**) are all part of *xvr*. (C) Our patient-specific neural networks achieve low initial pose estimation errors across all patients, whereas supervised methods exhibit high inter-subject variation and frequent out-of-distribution failures. (D and E) Survival curves of the final pose estimation error for various registration methods at multiple different success thresholds in DeepFluoro and Ljubljana, respectively. (F) Cumulative success rates for various registration rates quantified by the area under the survival curves demonstrate the superior performance of patient-specific models, whether trained from scratch or via finetuning. Finetuning via transfer learning is particularly important for Ljubljana as precise 3D/3D registration of patient-specific preoperative volumes to the pretraining dataset is more difficult for soft-tissue (vasculature) than bony structures (pelvic anatomy). (G) Initial pose estimates produced by the various pose estimation strategies for a particularly challenging intraoperative X-ray (*top*). The extreme cranial angle of this view is very far from a standard frontal view (*Fixed Initialization*). Therefore, such poses are severely underrepresented in the training set of real X-ray images, and thus, the supervised model (*Landmark Initialization*) suffers an out-of-distribution failure and predicts an implausible initial pose. In contrast, the patient-specific and finetuned models predict highly accurate initial pose estimates, which are quickly refined to yield a submillimeter accurate registration. Again, ground truth and estimated fiducial markers are only used for *post hoc* error visualization and error quantification, not during pose estimation.

Submillimeter-accurate iterative pose refinement with differentiable X-ray rendering (Fig. 4). The initial poses estimated by our patient-specific and finetuned neural networks are roughly 20 mm to 40 mm from the ground truth C-arm poses in both the DeepFluoro and Ljubljana datasets. However, high-stakes interventions often require intraoperative image guidance that is accurate within a few millimeters to ensure interventional success. Therefore, we further refine the pose estimates produced by the neural networks in *xvr* with rapid iterative optimization. Specifically, using our differentiable X-ray renderer, we maximize the similarity of the real intraoperative X-ray and the synthetic X-ray generated at the network-predicted pose with respect to the pose estimate using a gradient-based optimizer [65]. The details of our optimization scheme are provided in the Methods M.6.

Figure 4 reports the accuracy of *xvr* versus existing 2D/3D registration methods, evaluating multiple strategies for producing initial pose estimates and performing iterative pose refinement. Using the DeepFluoro dataset, we compared the self-supervised pose regression networks in *xvr* to two existing methods. First, we compared against *fixed initialization* [45], where the same manually selected initial pose is used for every X-ray from all patients (e.g., a standard frontal or lateral pose). While *fixed initialization* performs consistently across patients, it results in a high median error of 342.7 mm (IQR: 276.6 mm to 426.2 mm) as clinicians frequently acquire non-standard views during interventions. Next, we evaluated *landmark initialization* [54], a supervised deep learning method that trains a UNet [66] to estimate the location of manually annotated anatomical landmarks from 2D X-rays. These landmarks are then used to directly estimate the pose of the C-arm using the Perspective-n-Point algorithm [67]. This supervised neural network was evaluated using leave-one-out cross-validation, training a new model for each subset of five subjects and estimating the poses of X-rays from the held-out subject. *Landmark initialization* achieved a median pose estimation error of 52.1 mm (IQR: 30.8 mm to 98.5 mm), which was less accurate than our finetuned model (37.1 mm (IQR: 26.3 mm to 51.3 mm)).

Supervised learning with *landmark initialization* [54] also exhibited extremely high inter-subject variability compared to *xvr*. On the three most challenging subjects in DeepFluoro, *xvr* achieved median registration accuracies of 29.1 mm, 44.8 mm, and 26.5 mm, whereas *landmark initialization* achieved 64.5 mm, 81.4 mm, and 161.5 mm, respectively (Fig. 4C). Of note, *landmark initialization* incurs the highest error rates when the error of the *fixed initialization* is highest, demonstrating that supervised learning models perform poorly on non-standard acquisitions. For example, in Figure 4G, we visualize the initial pose estimates produced by various models from an unconventional intraoperative view. Such acquisitions are underrepresented in the limited samples of real X-rays available for supervised training. As such, *landmark initialization* suffers an out-of-distribution failure. Although this safety risk is inherent to supervised models, our patient-specific framework mitigates this problem by being trained exclusively on the patient undergoing the procedure with ample synthetic data.

For each method in Figure 4A and B, we report the training time and the submillimeter success rate (SMSR), defined as the percentage of X-ray images successfully registered with mTRE less than 1 mm following pose refinement. The most accurate methods were *xvr* initialized with either our *de novo* or finetuned neural networks, achieving SMSRs of 42.9% and 44.0% on DeepFluoro, respectively. The *de novo* model required 12 h of inpatient training time, while the finetuned model only needed 5 min of training to achieve equivalently accurate final pose estimates. Remarkably, initializing iterative optimization with our patient-agnostic neural network (pretrained on CTPelvic1K) achieved 41.5% SMSR after 48 h of offline training (Fig. 4A). This demonstrates that patient-agnostic pretraining is still useful in real-world clinical scenarios that cannot allow for any inpatient training time. In contrast, iterative optimization with differentiable rendering from a *fixed initialization*, another method that requires no patient-specific training, only achieved an SMSR of 7.6%.

To evaluate the utility of differentiable rendering, we also compared against iterative optimization performed using xReg, a gradient-free pose refinement method [54]. Gradient-free optimization failed to achieve robustly accurate final pose estimates, producing SMSRs of 0.3% and 3.3% for the *fixed* [45] and *landmark initializations* [54], respectively (Fig. 4A). *Landmark regularization* [54], which uses predicted 2D landmarks as an additional loss term during iterative optimization from the fixed initialization, achieved an SMSR of 1.7%. These results highlight the utility of gradient-based optimization in achieving submillimeter-accurate pose estimates for 2D/3D registration.

Another disadvantage of supervised landmark-based models is that their architectures typically do not extend to novel anatomical structures. For example, in Ljubljana, there are no segmentation masks from which to regress annotated landmarks, so landmark localization is not feasible with the UNet model proposed in [54]. Furthermore, the neurovasculature is a highly heterogeneous anatomical structure, so much so that population-level landmark detection not necessarily feasible [68]. Lastly, the small sample size of the Ljubljana dataset ($n = 20$ X-rays) makes it unlikely that any supervised model trained on these data would successfully generalize. In comparison, our image-based pose regression approach extends directly to Ljubljana. On this novel dataset, *xvr* also performed well, achieving 25% SMSR after 5 min of patient-specific finetuning time (Fig. 4B).

In addition to reporting SMSR, we evaluated the success of our registrations at different thresholds. For example, for many orthopedic procedures, registration within 10 mm may be considered successful [45]. To evaluate the cumulative success rate, we plotted the survival curves of the final pose estimates for all methods over varied thresholds (Fig. 4D and E). These curves demonstrate the uniform superiority of patient-specific registration over previous approaches. Finally, by calculating the normalized area under these survival curves (AUC), we quantified the cumulative success of various registration methods (Fig. 4F). Our *de novo* and finetuned networks achieved the highest AUC on DeepFluoro (0.80 vs. 0.80) and Ljubljana (0.84 vs. 0.83).

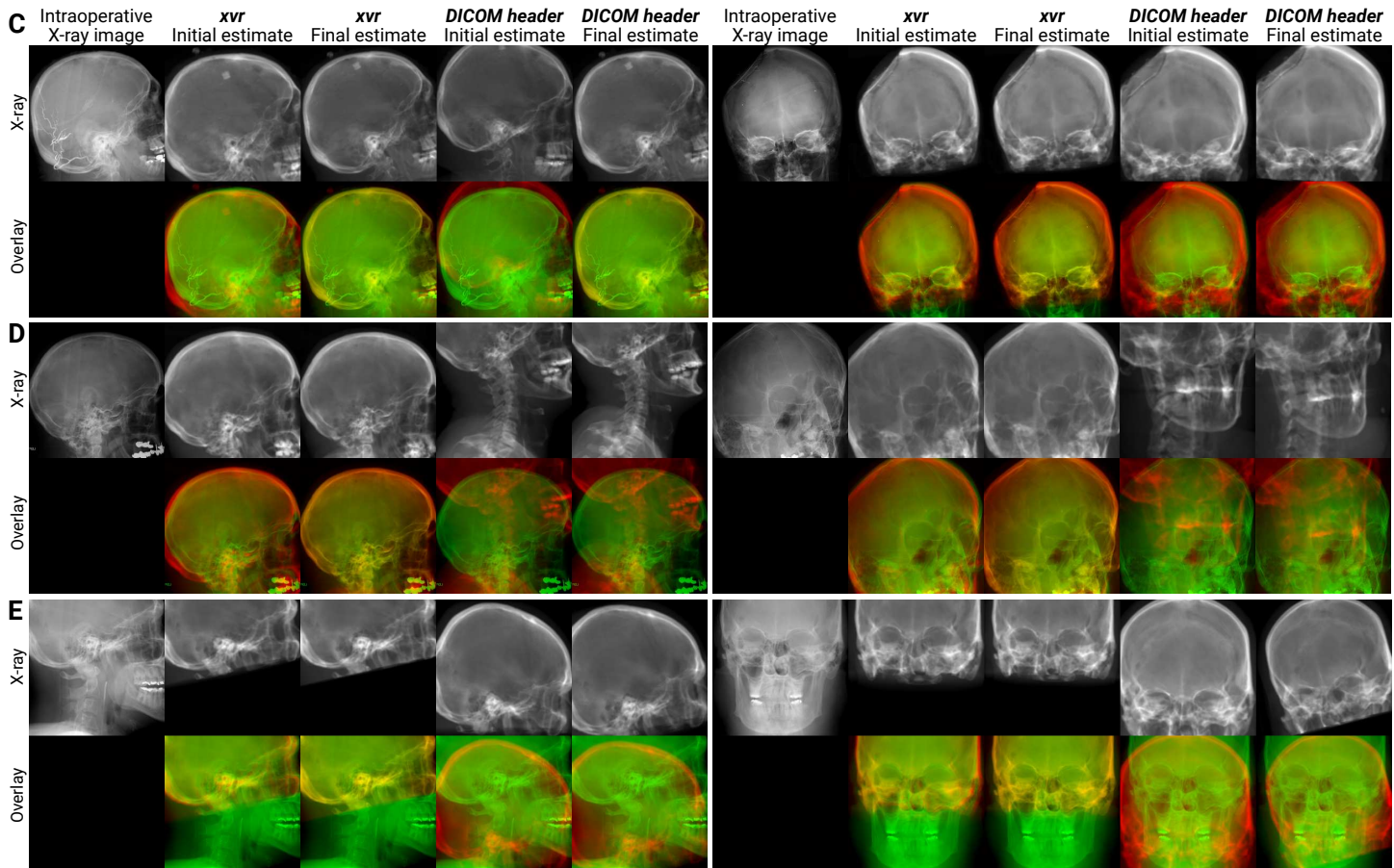
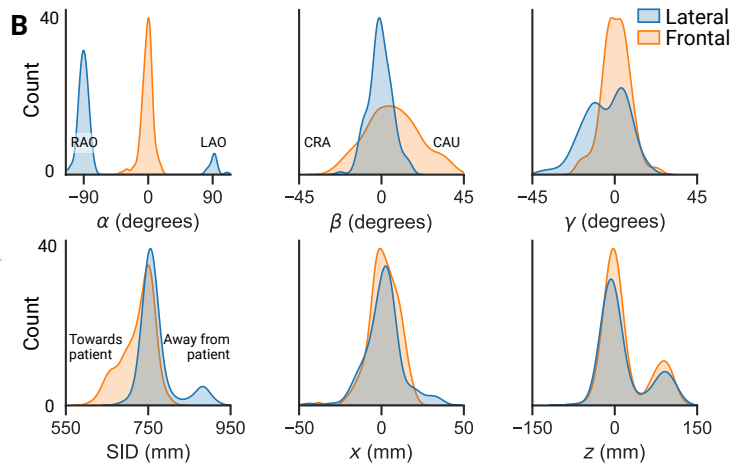
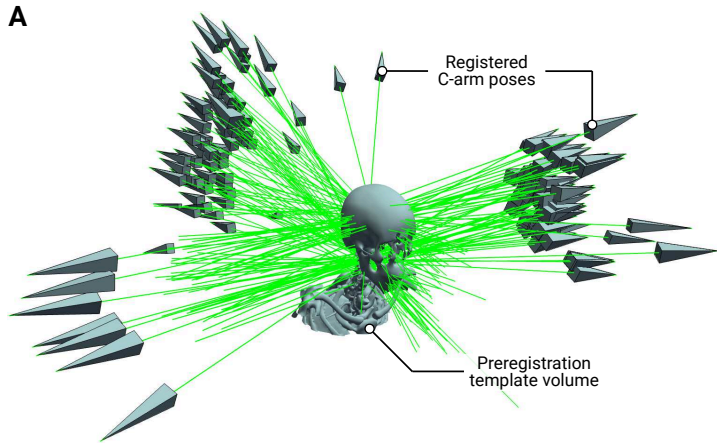
A

Figure 5. xvr enables the rapid registration of large volumes of real-world clinical data. (A) A patient-agnostic pose estimation model was trained using synthetic X-rays rendered from 61 preregistered head CTs in the TotalSegmentator dataset. Using this model and iterative pose refinement, 122 intraoperative X-rays acquired from 50 neurosurgical patients at Brigham and Women's Hospital were registered to their corresponding preoperative 3D imaging. Registered C-arm poses from all 122 X-rays are visualized relative to the template head CT used for 3D preregistration. (B) Distributions of the estimated pose parameters reveal interesting clinical patterns, e.g., right anterior oblique (RAO) lateral X-rays are acquired 8× more frequently in this dataset than left anterior oblique (LAO) X-rays. (C–E) From manual evaluations by trained neuroradiologists and neurointerventionalists, registrations produced by xvr achieved a higher average success rate (96.2%) compared to registrations initialized from pose parameters in the DICOM header (30.5%). (C) xvr's neural network retains its accuracy even when tested on intraoperative images containing interventional findings, such as embolized vessels or craniotomies, which are not represented in the pretraining dataset. (D) Pose parameters provided in the DICOM header do not account for the motion of the patient relative to the C-arm, which often leads to insurmountably high initial pose estimation error. In contrast, xvr produces consistently accurate initial pose estimates, even for unconventional views. (E) Compared to CTs in benchmark datasets, clinical CTs sometimes contain smaller fields-of-view so as to limit radiation exposure. Even with this limitation, xvr can still register partial CT renders to full field-of-view X-rays. From these registrations, soft tissue findings encased within the skull's rigid structure (e.g., the location of a tumor or hemorrhage) can be reprojected from CT onto intraoperative X-rays for augmented image guidance.

Scaling to real-world clinical datasets (Fig. 5). To demonstrate *xvr*’s effectiveness on large clinical datasets from high-volume centers, we registered CT volumes and X-ray images from 50 neurosurgical patients at Brigham and Women’s Hospital. In total, this dataset comprised 50 contrast-enhanced CT angiograms (CTAs) and 122 DSAs from frontal and lateral views acquired using biplane C-arm scanners.

To register these data, we first trained a patient-agnostic pose estimation model for skull radiographs using *xvr*. Specifically, we pretrained on synthetic X-rays generated from 61 head CTs in the TotalSegmentator dataset [69]. Then, given a DSA from the clinical dataset, we extracted the first frame before subtraction to highlight bony craniofacial structures, resampled the X-ray using the network’s fixed intrinsic parameters (Fig. S2), and processed the frame using the patient-agnostic model. We then automatically corrected the network-estimated C-arm pose by rigidly registering the corresponding patient’s CTA to the preregistration template from the TotalSegmentator dataset. Finally, these initial pose estimates were refined using our iterative optimizer.

Registered C-arm poses were visualized relative to the pre-registration template volume (Fig. 5A) alongside distributions of the recovered pose parameters (Fig. 5B). For comparison, we also performed iterative optimization initialized from the C-arm pose encoded in the DICOM header (see the Methods M.7). However, these parameters fail to account for the positioning of the patient relative to the C-arm, resulting in highly inaccurate registrations (see the fourth columns in Fig. 5C–E). Unlike the benchmark datasets, the clinical X-rays in this dataset were not accompanied by calibrated ground truth C-arm poses. Therefore, all registration results were manually inspected by a neuroradiologist and a neurointerventionalist who were blinded to the initialization method. *xvr* yielded accurate alignment in all cases in the neuroradiologist’s assessment, whereas DICOM-initialization only succeeded in 39.7% of cases. In the neurointerventionalist’s evaluation, *xvr*- and DICOM-initialization produced successful alignments in 92.6% and 21.4% of cases, respectively.

This clinical dataset also contained novel domain shifts between the 2D and 3D imaging. For example, some intraoperative DSAs captured the results of surgical interventions, such as embolized blood vessels or craniotomies (Fig. 5C). These findings were not present in preoperative volumes and, thus, not represented in the synthetic X-rays with which the model was trained nor those used to drive pose refinement. Despite this, our patient-agnostic model and optimization scheme produced accurate initial and final pose estimates, respectively, highlighting the robustness of *xvr* to interventional changes. In addition, many clinical CTAs image only a portion of the skull to minimize radiation exposure. Renderings from these CTAs resulted in synthetic X-rays that only partially aligned with the real X-rays (Fig. 5E). However, even when given a partial volume, the pose refinement protocol in *xvr* produced accurate alignments. Finally, registering this large volume of clinical data with *xvr* was remarkably efficient, requiring only 10 min for the entire dataset. The speed and accuracy of *xvr* enables the development of new image-guidance systems that rely on 2D/3D registration.

3 Discussion

The registration of intraoperative 2D X-rays to 3D preoperative scans is a prerequisite for numerous surgical procedures and emerging AI-based technologies that aim to improve the state-of-the-art in image-guided interventions [22–25, 28–31]. However, existing 2D/3D registration methods have so far failed to deliver consistent performance across diverse patient populations and clinical practices [32]. As even millimeter-level inaccuracies in a model’s predictions can lead to catastrophic outcomes [58, 59], interventional settings cannot yet integrate these tools due to the safety and robustness issues affecting current models. To address these challenges, we developed *xvr*, a self-supervised machine learning framework that enables the rapid training of neural networks for X-ray to volume registration individualized to a subject’s own anatomy. Our approach provides reliable, accurate, and anatomically generic 2D/3D registration across multiple medical specialties.

Solving the data bottleneck. *xvr* leverages routinely acquired preoperative 3D imaging to drive a patient-specific simulation for training self-supervised pose regression networks (Fig. 1). Using our physics-based differentiable renderer, we generate synthetic X-rays that maintain high fidelity to real X-rays in both appearance and geometry (Fig. 2E and F). We demonstrate that networks trained exclusively on these synthetic X-rays successfully generalize to real intraoperative images (Fig. 3C and D). This approach stands in contrast to existing supervised deep learning methods for C-arm pose estimation, which are limited by the scarcity of intraoperative X-rays with ground truth poses, hampering their generalization and robustness. Furthermore, current landmark-based pose estimation networks [70] burden interventionalists by requiring manual annotation of fiducial landmarks for each new patient, making such methods only semi-automatic. By eliminating the need for manual annotations or ground truth poses, our approach better integrates patient-specific model training into existing clinical workflows without disruption or additional burden.

Improving generalization capabilities. Supervised models are overfit to subjects in their training set and are frequently unable to generalize to new patients, procedures, or pathologies. As we observe in our analyses, supervised registration methods trained with this “one-model-fits-all” approach exhibit high inter-subject variability (Fig. 4). Like supervised pose estimation models, our patient-specific models are also extremely overfit. However, *this is intentional*. Instead of overfitting to subjects in an arbitrary training set, we design our models to overfit to the specific patient undergoing the intervention. By learning the specific appearance and geometry of a patient’s anatomy from synthetic X-rays, *xvr* achieves state-of-the-art 2D/3D registration accuracy, outperforming existing methods by an order of magnitude (Fig. 4). Furthermore, by implementing a comprehensive data augmentation pipeline (Fig. S1), *xvr* is robust to intraoperative domain shifts, such as the patient changing their position between pre- and intraoperative image acquisition or the appearance of medical devices (Fig. 5).

Training patient-specific networks in just 5 min. `xvr` also addresses a long-standing limitation of patient-specific models: their extensive training time. By first pretraining patient-agnostic models on publicly available volumetric datasets, `xvr` reduces the time required to train an accurate patient-specific model from hours in previous work [53] to just 5 min using transfer learning (Fig. 3). This strategy is highly flexible and robust to significant domain shifts between the volumes used for pretraining and the volumes acquired clinically. For example, CTPelvic1K comprises whole-pelvis scans containing many clinical findings, while DeepFluoro volumes do not contain the top half of the torso (Fig. 3A). NITRC MRAs, in addition to being a completely different modality, are of healthy volunteers whereas 3D rDSAs in Ljubljana contain vascular malformations (Fig. 3B). Furthermore, the relative simplicity of pelvic anatomy makes it easy to correct the pose estimates from a patient-agnostic model with 3D rigid registration, while Ljubljana is forced to rely on center alignment, which is effectively anatomy-agnostic.

Despite these numerous challenges, patient-agnostic models pretrained on these datasets transfer well to real X-ray images in DeepFluoro and Ljubljana, demonstrating that this multi-patient simulation helps a pose regression network learn the geometry of human anatomy at a population level (Fig. 4). This hypothesis is further supported by the speed with which this pretrained model can be finetuned on a new subject. In total, these experiments demonstrate that the introduction of a patient-agnostic model amortizes the preoperative time required to train a patient-specific neural network. Our findings improve the feasibility of patient-specific machine learning in real clinical settings, thereby extending its applicability to a broader range of fluoroscopy-guided surgical domains, such as emergency interventions or settings without preoperative imaging.

Limitations and future work. The success of `xvr` across multiple surgical datasets naturally suggests many avenues for future work. For example, `xvr` achieves submillimeter registration accuracy through a carefully designed iterative pose refinement protocol (further described in the Methods M.6). Pose refinement is necessary as the accuracy of the initial pose estimates regressed by neural networks in `xvr` is between 20 mm to 40 mm, which is the current state-of-the-art. Although iterative solvers currently showcase better performance over deep learning estimators in multiple medical image registration domains [71–73], improving the accuracy of deep learning estimators is highly sought-after as they yield predictions in milliseconds. For example, achieving *real-time* submillimeter-accurate pose estimates without iterative refinement is crucial to power fully interactive autonomous surgical robotics, *e.g.*, self-driving image-guidance systems [74, 75]. This can potentially be achieved by incorporating iterative optimization in the simulated training task, *e.g.*, with model-agnostic meta-learning [76] or deep equilibrium models [77, 78]. Additionally, `xvr` does not directly address the need for non-rigid 2D/3D registration of fully deformable anatomical structures, *e.g.*, the lungs or the abdomen. As many interventional radiology procedures for these organs

would benefit from the same level of accuracy that we have achieved for rigid 2D/3D registration (*e.g.*, image-guided needle biopsies), adapting `xvr` to perform non-rigid registration is an exciting future direction.

4 Conclusion

`xvr` is a fully automatic machine learning framework for patient-specific 2D/3D registration. On the largest evaluation of a 2D/3D registration method on real data to date, `xvr` achieves consistently accurate image alignment for all patients comprising numerous anatomical structures, diseases, and image acquisition setups. `xvr` further contributes many engineering developments to the field of 2D/3D registration, including a fast differentiable X-ray renderer for gradient-based pose refinement (Fig. 2) and a simple command line interface that allows practitioners to train their own pose regression models and register large clinical datasets in minutes. Through the sum of these contributions, `xvr` aims to eliminate 2D/3D registration as a bottleneck to the development of next-generation X-ray image guidance technologies. `xvr` is freely available at <https://github.com/eigenvivek/xvr>.

Data availability

We used the following publicly available 2D/3D registration datasets:

- DeepFluoro (<https://github.com/rg2/DeepFluoroLabeling-IPCAI2020>)
- Ljubljana (<https://lit.fe.uni-lj.si/en/research/resources/3D-2D-GS-CA>)

Remixed versions of these datasets into the DICOM format are available, with permission from the original authors, at <https://huggingface.co/datasets/eigenvivek/xvr-data>. We used the following publicly available 3D imaging datasets:

- CTPelvic1K (<https://github.com/MIRACLE-Center/CTPelvic1K>)
- NITRC MRA Atlas (<https://www.nitrc.org/projects/icbmrra>)
- TotalSegmentator (<https://github.com/wasserth/TotalSegmentator>)

Due to Health Insurance Portability and Accountability Act (HIPAA) regulatory requirements, the Brigham CTA/DSA dataset remains unavailable for public release at this time.

Code availability

The Python package and command line interface for `xvr`, along with all scripts necessary to replicate the experiments presented in this manuscript, are available at <https://github.com/eigenvivek/xvr>. Pretrained patient-agnostic, patient-specific, and finetuned model weights are available at <https://huggingface.co/eigenvivek/xvr>. `xvr` is implemented in Python 3.10+ and uses PyTorch 2.2+ [79] as its automatically differentiable backend.

Acknowledgments

We are grateful to Theo van Walsum for explaining to us how C-arm poses are parameterized in DICOM headers. This work was supported by NIH NIBIB 5T32EB001680-19.

Methods

M.1 Differentiable X-ray rendering. We first describe the coordinate system implemented in our X-ray renderer, detailing how the pose of the C-arm relative to the 3D volume are determined. Then, using the X-ray image formation model, we derive the rendering equations computed by in our model from first principles. Finally, we present two differentiable algorithms implemented in `xvr` to approximate the rendering equation with discrete 3D volume and discuss their utility in tomographic optimization problems. Our renderer is implemented in PyTorch, which means that all rendering operations are differentiable and easily integrated into deep learning architectures as a neural network layer.

Geometry of the 3D volume. The physical spacing and orientation of the 3D volume is determined by its affine matrix \mathbf{A} , which maps voxel coordinates $(i, j, k) \in \mathbb{N}^3$ to world coordinates $(x, y, z) \in \mathbb{R}^3$, represented in homogeneous coordinates:

$$\mathbf{A} = \begin{bmatrix} \Delta x & 0 & 0 & O_x \\ 0 & \Delta y & 0 & O_y \\ 0 & 0 & \Delta z & O_z \\ 0 & 0 & 0 & 1 \end{bmatrix}, \quad (1)$$

where $\mathbf{O} = (O_x, O_y, O_z)$ is the origin of the 3D volume in world coordinates and $\Delta = (\Delta x, \Delta y, \Delta z)$ is the spacing in each voxel dimension with units of millimeters per voxel. The signs of the elements in Δ determine the orientation of the 3D volume along each of the axes. If the number of pixels in each dimension of the 3D is $\mathbf{N} = (N_x, N_y, N_z)$, then the patient's isocenter in world coordinates is

$$\mathbf{i} = \frac{\mathbf{N} \odot \Delta}{2} + \mathbf{O}, \quad (2)$$

where \odot is the Hadamard product, representing element-wise multiplication.

Geometry of the C-arm. We follow the standard approach of modeling a C-arm as a pinhole camera, allowing us to mathematically express the X-ray image formation model using projective geometry. The intrinsic matrix \mathbf{K} , which maps camera coordinates to pixel coordinates [80], can be decomposed as

$$\mathbf{K} = \begin{bmatrix} 1/s_x & 0 & W/2 \\ 0 & 1/s_y & H/2 \\ 0 & 0 & 1 \end{bmatrix} \begin{bmatrix} f & 0 & o_x \\ 0 & f & o_y \\ 0 & 0 & 1 \end{bmatrix} = {}^P\mathbf{K}_I {}^I\mathbf{K}_C, \quad (3)$$

where f is the C-arm's source-to-detector distance (i.e., the focal length) in millimeters, (o_x, o_y) is the optical center of the C-arm in millimeters, (s_x, s_y) are the spacings of pixels in the detector plane with units of millimeters per pixel, and (H, W) are the height and width in pixels of the detector plane. Note that ${}^I\mathbf{K}_C$ maps camera coordinates to image coordinates (with units of millimeters) and ${}^P\mathbf{K}_I$ maps image coordinates to pixel coordinates.

The X-ray source is initialized at the origin in world coordinates $(0, 0, 0)$ and the center of the detector plane is

initialized at $(0, 0, f)$, where the intrinsic parameters in \mathbf{K} determine the initial positions of the pixel centers in the detector plane. These initial positions are then reoriented such that the depth dimension of the renderer is aligned with either the posterior-anterior or anterior-posterior dimension of the CT scan (i.e., the y -axis). The positions of the X-ray source and detector can be reoriented using any 3D rigid transformation $\mathbf{T} \in \text{SE}(3)$, the special Euclidean group. Specifically, \mathbf{T} is composed of a 3D rotation $\mathbf{R} \in \text{SO}(3)$ and a 3D translation $\mathbf{t} \in \mathbb{R}^3$, which can be expressed in homogeneous coordinates as

$${}^W\mathbf{T}_C = \begin{bmatrix} \mathbf{R} & \mathbf{R}\mathbf{t} \\ \mathbf{0} & 1 \end{bmatrix}. \quad (4)$$

That is, \mathbf{T} determines the geometry of the C-arm by first translating the X-ray source and detector by \mathbf{t} , then rotating the camera's coordinate frame by \mathbf{R} . This transformation, often referred to in this paper as the C-arm pose or more generally as the camera-to-world matrix, can be composed with the intrinsic matrix \mathbf{K} to form the projection matrix

$$\mathbf{\Pi} = \mathbf{K}[\mathbf{R}^T \mid -\mathbf{t}], \quad (5)$$

which maps any point in world coordinates to pixel coordinates using a perspective projection. Note that in Eq. (5), points in world coordinates are first mapped to camera coordinates with the world-to-camera matrix:

$${}^C\mathbf{T}_W = \text{inv}({}^W\mathbf{T}_C) = \begin{bmatrix} \mathbf{R}^T & -\mathbf{t} \\ \mathbf{0} & 1 \end{bmatrix}. \quad (6)$$

There are many choices of parameterization for the rotation matrix \mathbf{R} , such as Euler angles, quaternions, the axis-angle parameterization, the tangent space $\mathfrak{so}(3)$, etc. `xvr` supports all of these parameterizations whether for specifying the position and orientation of the C-arm or performing gradient-based pose optimization. However, we emphasize that commercial C-arms define rotation matrices using Euler angles with the convention

$$\mathbf{R}(\alpha, \beta, \gamma) = \mathbf{R}_z(\alpha)\mathbf{R}_x(\beta)\mathbf{R}_y(\gamma), \quad (7)$$

where \mathbf{R}_i is a 3×3 matrix denoting rotation about the i -axis for $i \in \{x, y, z\}$. Here, α refers to the left-right anterior oblique rotational axis (LAO/RAO) and β refers to the cranial-caudal rotational axis (CRA/CAU), two common angles in diagnostic and interventional radiology. The geometric convention of commercial C-arms as implemented in `xvr` is illustrated in Fig. 1C.

Rendering equation. We present a derivation of the first-order model underlying X-ray image formation in a continuous form to inspire a discretized computational implementation. First, let $\mathbf{s} \in \mathbb{R}^3$ be the radiation point source and $\mathbf{p} \in \mathbb{R}^3$ be the target point of a pixel on the X-ray detector plane, both defined in world coordinates. These points define the ray $\vec{\mathbf{r}}(\alpha) = \mathbf{s} + \alpha(\mathbf{p} - \mathbf{s})$ for $\alpha \in [0, 1]$. This beam of high-energy photons is cast through a heterogeneous medium (e.g., human anatomy) $\mathbf{V} : \mathbb{R}^3 \mapsto [0, \infty)$, where $\mathbf{V}(\mathbf{x})$ represents the linear attenuation coefficient (LAC) at a point in the medium

	DeepFluoro				Ljubljana			
	mPE (2D)	mRPE (2.5D)	dGeo (3D)	mTRE (3D)	mPE (2D)	mRPE (2.5D)	dGeo (3D)	mTRE (3D)
Fixed init. (xReg) [45]	86.86 mm 18.0%	151.39 mm 18.7%	337.14 mm 0.3%	365.86 mm 0%			N/A	
Landmark reg. (xReg) [54]	0.96 mm 53.0%	2.24 mm 16.7%	3.16 mm 1.6%	4.31 mm 1.4%			N/A	
Landmark init. (xReg) [54]	0.93 mm 59.3%	1.96 mm 19.9%	2.86 mm 3.3%	3.85 mm 2.7%			N/A	
Fixed init. (xvr) [38]	74.97 mm 10.7%	137.57 mm 9.6%	277.77 mm 7.9%	354.85 mm 7.6%	10.88 mm 30%	129.55 mm 25%	149.85 mm 10%	149.9 mm 10%
Patient-agnostic (xvr)	0.18 mm 91.3%	0.64 mm 68.9%	0.94 mm 53.8%	1.16 mm 41.5%	23.51 mm 45%	40.10 mm 25%	57.27 mm 5%	45.10 mm 15%
Patient-specific (xvr)	0.18 mm 92.6%	0.59 mm 67.8%	0.92 mm 54.9%	1.10 mm 42.9%	0.63 mm 100%	0.94 mm 55%	1.30 mm 20%	1.40 mm 30%
Finetuned (xvr)	0.17 mm 92.3%	0.61 mm 68.9%	0.90 mm 55.5%	1.10 mm 44.0%	0.62 mm 100%	1.03 mm 45%	1.35 mm 25%	1.48 mm 25%

Table S1: Pose estimation error for various 2D/3D registration error metrics reported as the median error (mm) and submillimeter success rate (%). The dimensions in which error is measured is annotated and the best-performing 2D/3D registration method for each metric is bolded. Mean target registration error (mTRE), the most stringent metric, is reported throughout the main text.

$\mathbf{x} \in \mathbb{R}^3$. Then, the pixel intensity induced by this ray is given by the Beer-Lambert law:

$$I_{BL}(\vec{r}) \triangleq I_0 \exp \left(- \int_{\mathbf{x} \in \vec{r}} \mathbf{V}(\mathbf{x}) d\mathbf{x} \right) \quad (8)$$

$$= I_0 \exp \left(- \int_0^1 \mathbf{V}(\vec{r}(\alpha)) \|\vec{r}'(\alpha)\| d\alpha \right) \quad (9)$$

$$= I_0 \exp \left(- \|\mathbf{p} - \mathbf{s}\| \int_0^1 \mathbf{V}(\mathbf{s} + \alpha(\mathbf{p} - \mathbf{s})) d\alpha \right), \quad (10)$$

where I_0 is the initial intensity of the X-ray beam. To simplify the forward model, we can express the log-transformed version of this quantity

$$I(\vec{r}) \triangleq \log I_0 - \log I_{BL}(\vec{r}) \quad (11)$$

$$= \|\mathbf{p} - \mathbf{s}\| \int_0^1 \mathbf{V}(\mathbf{s} + \alpha(\mathbf{p} - \mathbf{s})) d\alpha. \quad (12)$$

Given an X-ray source $\mathbf{s} \in \mathbb{R}^3$ and a set of target pixels on the detector grid $\mathbf{P} \in \mathbb{R}^{n \times 3}$, we can reorient \mathbf{s} and \mathbf{P} by a rigid transform \mathbf{T} to render an X-ray from any particular view. Therefore, we denote the rendered image by $\mathbf{I} = \mathcal{P}(\mathbf{T}) \circ \mathbf{V}$, where \mathcal{P} is the projection operator in Eq. (11).

When rendering synthetic X-rays, we do not have access to the continuous form of \mathbf{V} . Instead, we have a discrete version from a preoperative 3D CT or MR volume. Therefore, computational modeling of X-ray image formation requires numerical methods to analytically compute the integral in Eq. (11). The first integration technique we consider is Siddon's method [56], which exactly computes a discretized version of Eq. (11) as the sum of the linear attenuation coefficient in each voxel on the path of \vec{r} , weighted by the intersection length of \vec{r} with each voxel. That is, $I(\vec{r})$ is exactly expressed as

$$\|\mathbf{p} - \mathbf{s}\| \sum_{m=1}^{M-1} \mathbf{V} \left[\mathbf{s} + \frac{\alpha_{m+1} + \alpha_m}{2} (\mathbf{p} - \mathbf{s}) \right] (\alpha_{m+1} - \alpha_m), \quad (13)$$

where $\{\alpha_1, \dots, \alpha_M\}$ parameterizes the intersection of \vec{r} with the parallel planes comprising \mathbf{V} as determined by the volume's affine matrix \mathbf{A} . Additionally, $\mathbf{V}[\cdot]$ is an indexing operation that returns the linear attenuation coefficient of the intersected voxel (*i.e.*, nearest-neighbor interpolation). We have previously shown that Eq. (13) can be implemented in a completely differentiable manner [38].

Instead of computing every plane intersection, which scales cubically with the resolution of \mathbf{V} , we can approximate the Beer-Lambert law using interpolatory quadrature. Thus, the second integration technique we consider uses trilinear interpolation to estimate $I(\vec{r})$ as

$$\|\mathbf{p} - \mathbf{s}\| \sum_{m=1}^{M-1} \mathbf{V}[\mathbf{s} + \alpha_m(\mathbf{p} - \mathbf{s})] \frac{(\alpha_{m+1} - \alpha_{m-1})}{2}, \quad (14)$$

where $\{\alpha_1, \dots, \alpha_M\}$ parameterize M evenly spaced points along \vec{r} and $\mathbf{V}[\cdot]$ represents trilinear interpolation. Trilinear interpolation is linear in M and thus faster and less computationally expensive than Siddon's method. Therefore, to increase batch sizes for neural network training and decrease rendering time for iterative pose refinement, we use trilinear interpolation for all tasks that require rendering synthetic X-rays in `xvr` by default.

In our renderer, both Siddon's method Eq. (13) and trilinear interpolation Eq. (14) are implemented in PyTorch. Therefore, these forward models are differentiable with respect to both the input pose \mathbf{T} and the volume \mathbf{V} . We have previously used differentiability with respect to \mathbf{V} to perform 3D cone-beam computed tomography reconstruction from multiple 2D X-rays [81]. Here, we exploit the differentiability to optimize an unknown pose \mathbf{T} .

M.2 Pose estimation error metrics (Tab. S1). There exist many metrics to assess the accuracy of 2D/3D registration results. In this section, we derive previously proposed 2D/3D registration metrics and use them to evaluate the DeepFluoro

	Rotations (°)						Translations (mm)					
	α_{\min}	α_{\max}	β_{\min}	β_{\max}	γ_{\min}	γ_{\max}	x_{\min}	x_{\max}	y_{\min}	y_{\max}	z_{\min}	z_{\max}
Pelvis	-45	45	-45	45	-15	15	-150	150	-450	-1000	-150	150
Neurovasculature	-45	90	-5	5	-5	5	-25	25	700	800	-25	25
Skull	-125	125	-45	45	-15	15	-200	200	-500	-1000	-200	200

Table S2: Minimum and maximum pose parameter used to train both patient-specific and patient-agnostic models for every anatomical structure. The correspondences between anatomical structures and datasets are as follows: pelvis (DeepFluoro and CTPelvic1K), neurovasculature (Ljubljana and NITRC MRA), and skull (Brigham and TotalSegmentator).

and Ljubljana datasets (Tab. S1). Throughout the main text, we report mean Target Registration Error (mTRE) as it is the most stringent of all metrics we consider.

Preliminaries. Let $\mathbf{T}, \hat{\mathbf{T}} \in \text{SE}(3)$ be a ground truth and estimated C-arm pose. Additionally, let \mathbf{K} be the known intrinsic matrix for C-arm, which we combine with the C-arm poses to make the projection matrices $\mathbf{\Pi}, \hat{\mathbf{\Pi}}$ using Eq. (5). Finally, let $\mathbf{X} \in \mathbb{R}^{3 \times M}$ be a collection of M fiducial markers annotated for every volume. In projective geometry, 3D points are typically represented using homogeneous coordinates in order to represent perspective projections with a single matrix operation [80]. Specifically, we use $\pi(\mathbf{X}) = \mathbf{x} \in \mathbb{R}^2$ to represent the following nonlinear operation:

$$\mathbf{\Pi} \begin{bmatrix} X \\ Y \\ Z \\ 1 \end{bmatrix} = \begin{bmatrix} x \\ y \\ z \end{bmatrix} \in \mathbb{P}^2 \longrightarrow \mathbf{x} = \begin{bmatrix} x/z \\ y/z \end{bmatrix} \in \mathbb{R}^2. \quad (15)$$

Mean Projection Error (mPE). This metric measures the distance between fiducials when projected onto the ground truth and estimated detector planes (*i.e.*, in 2D):

$$\mathcal{L}_{\text{mPE}}(\mathbf{T}, \hat{\mathbf{T}}) = \frac{1}{M} \|\pi(\mathbf{X}) - \hat{\pi}(\mathbf{X})\|_2. \quad (16)$$

Mean Reprojection Error (mRPE). This metric lifts 2D projected fiducials onto a 2D plane in 3D. This enables measurement of the distance between the detector planes (*i.e.*, in 2.5D):

$$\mathcal{L}_{\text{mRPE}}(\mathbf{T}, \hat{\mathbf{T}}) = \frac{1}{M} f \|\mathbf{K}^{-1}(\pi(\mathbf{X}) - \hat{\pi}(\mathbf{X}))\|_2, \quad (17)$$

where f is the focal length of the C-arm, derived from \mathbf{K} .

Double geodesic distance. The distance between two extrinsic camera poses can be decomposed into rotational and translational distances:

$$\mathcal{L}_{\text{rot}}(\mathbf{R}, \hat{\mathbf{R}}) = \arccos \left(\frac{\text{tr}(\mathbf{R}^T \hat{\mathbf{R}}) - 1}{2} \right) \quad (18)$$

$$\mathcal{L}_{\text{arc}}(\mathbf{R}, \hat{\mathbf{R}}) = \frac{f}{2} \mathcal{L}_{\text{rot}}(\mathbf{R}, \hat{\mathbf{R}}) \quad (19)$$

$$\mathcal{L}_{\text{xyz}}(\mathbf{t}, \hat{\mathbf{t}}) = \|\mathbf{t} - \hat{\mathbf{t}}\|_2, \quad (20)$$

where multiplying Eq. (18) by the radius $f/2$ converts arc length from units of radians to millimeters. Finally, these metrics can be combined into a single distance metric:

$$\mathcal{L}_{\text{dGeo}}(\mathbf{T}, \hat{\mathbf{T}}) = \sqrt{\mathcal{L}_{\text{arc}}(\mathbf{R}, \hat{\mathbf{R}})^2 + \mathcal{L}_{\text{xyz}}(\mathbf{t}, \hat{\mathbf{t}})^2}. \quad (21)$$

Note that, unlike the other three metrics described in this section, $\mathcal{L}_{\text{dGeo}}$ does not depend on the existence of manually annotated fiducials. Therefore, we use Eq. (21) as a loss function when training pose regression neural networks in xvr ; see Eq. (24).

Mean Target Registration Error (mTRE). This metric directly measures the distance between fiducial markers in world coordinates, ignoring the projection (*i.e.*, in 3D):

$$\mathcal{L}_{\text{dGeo}}(\mathbf{T}, \hat{\mathbf{T}}) = \frac{1}{M} \|(\mathbf{T} - \hat{\mathbf{T}})\tilde{\mathbf{X}}\|_2, \quad (22)$$

where $\tilde{\mathbf{X}} \in \mathbb{P}^3$ are the fiducial markers in homogeneous coordinates.

M.3 Patient-specific neural network training. We train a patient-specific pose regression network using synthetic X-rays rendered from the patient's preoperative volume. To do this, we first sample random C-arm poses from a distribution over plausible angles that may be acquired intraoperatively. Specifically, we sample individual pose parameters from the uniform distributions

$$\begin{aligned} \alpha &\sim \text{Uniform}[\alpha_{\min}, \alpha_{\max}] & x &\sim \text{Uniform}[x_{\min}, x_{\max}] \\ \beta &\sim \text{Uniform}[\beta_{\min}, \beta_{\max}] & y &\sim \text{Uniform}[y_{\min}, y_{\max}] \\ \gamma &\sim \text{Uniform}[\gamma_{\min}, \gamma_{\max}] & z &\sim \text{Uniform}[z_{\min}, z_{\max}], \end{aligned}$$

and combine parameters into a single pose \mathbf{T} , where the rotation matrix \mathbf{R} is given by Eq. (7) and the translation is defined as $\mathbf{t} = [x \ y \ z]^T$. The parameter ranges we use when training models for various anatomical structures are provided in Tab. S2.

Given a batch of random C-arm poses \mathbf{T}_n , we generate a batch of random synthetic images

$$\mathbf{I}_n = \mathcal{P}(\mathbf{T}_n) \circ \mathbf{V} \quad \forall n \in \{1, \dots, N\}, \quad (23)$$

using our differentiable X-ray renderer (Fig. S1A). After generating these synthetic images, we execute the following training loop (Fig. S1B): First, the batch of images is passed to a convolutional neural network $f_{\theta} : \mathcal{I} \mapsto \text{SE}(3)$, which regresses a C-arm pose from each image $\hat{\mathbf{T}}_n = f_{\theta}(\mathbf{I}_n)$. These predicted poses are then passed back to our renderer to generate estimated X-rays $\hat{\mathbf{I}}_n = \mathcal{P}(\hat{\mathbf{T}}_n) \circ \mathbf{V}$. Finally, these estimated C-arm poses and X-rays can be compared to the ground truth values produced via simulation to compute a loss function for the neural network:

$$\mathcal{L}(\theta) = \frac{1}{N} \sum_{n=1}^N \left(\lambda \mathcal{L}_{\text{dGeo}}(\mathbf{T}_n, \hat{\mathbf{T}}_n) + \mathcal{L}_{\text{mNCC}}(\mathbf{I}_n, \hat{\mathbf{I}}_n) \right), \quad (24)$$

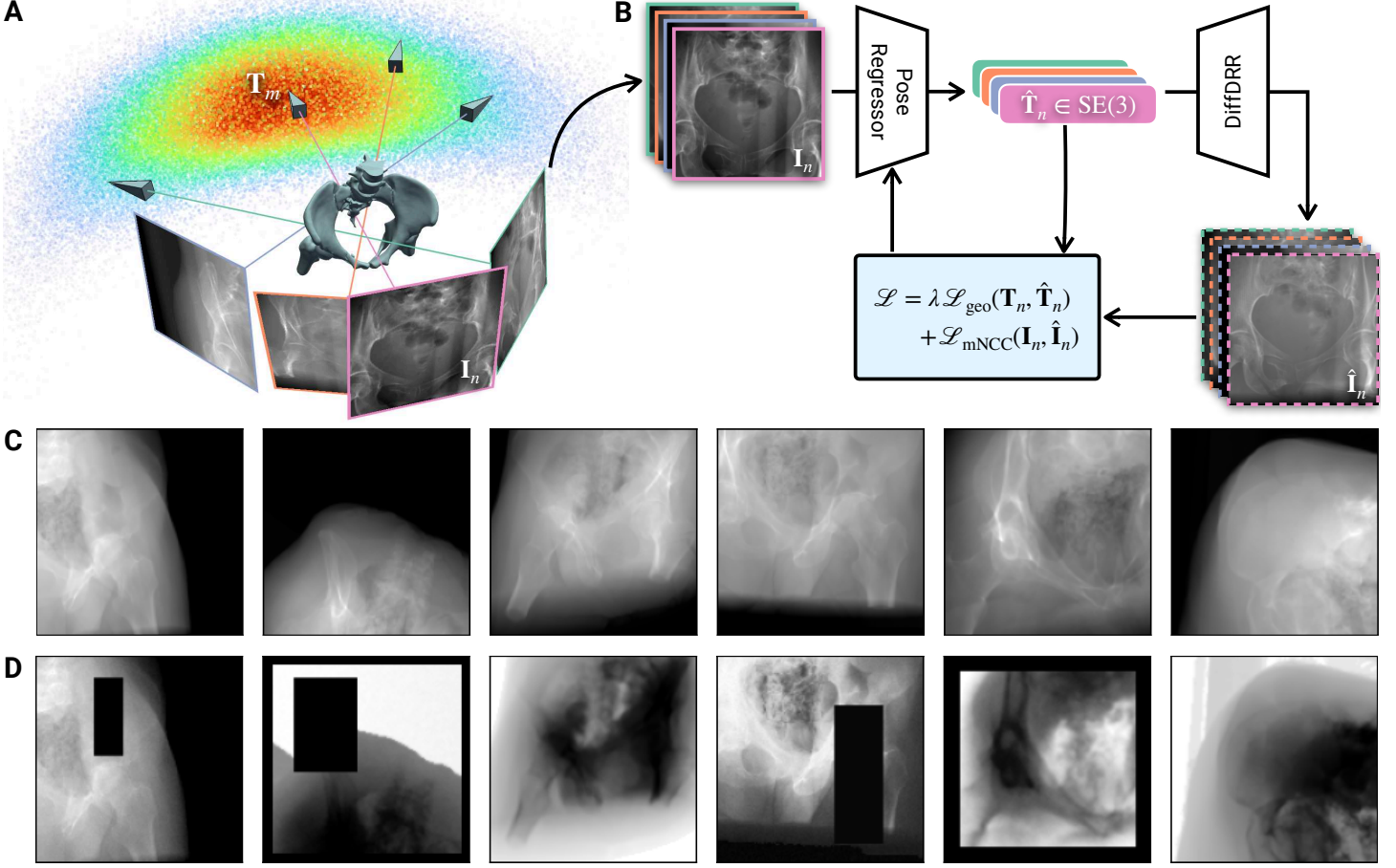


Figure S1. Patient-specific simulated training task. (A) Given a preoperative volume of a patient, we generate patient-specific synthetic X-rays \mathbf{I}_n from random camera poses \mathbf{T}_n using our X-ray renderer. (B) These synthetic X-rays are then passed to a pose regression network, which regresses an estimated camera pose $\hat{\mathbf{T}}_n$ for each input X-ray. These estimated camera poses can then be passed again to our renderer to generate estimated images $\hat{\mathbf{I}}_n$. All these estimated quantities can be compared to their ground truth counterparts, which we can access since they are simulated, to form our composite pose regression loss. This loss function is then used to optimize the pose regression network with gradient descent. (C) Example synthetic X-rays rendered at random C-arm poses from the preoperative imaging. (D) To improve the robustness of the pose estimation network, we perform data augmentations such as adding Gaussian noise, inverting the images, and masking rectangular patches or simulating collimation.

where $\mathcal{L}_{d\text{Geo}}$, the double geodesic distance between two poses in $\text{SE}(3)$, is given in Eq. (21) and mNCC is multiscale normalized cross correlation [53], and we set $\lambda = 10^{-2}$.

Data augmentation. In Fig. S1C, we visualize a batch of synthetic X-rays rendered from the CT scan of a subject in the DeepFluoro dataset. During training, we heavily augment these images to simulate various intraoperative aberrations. We apply various intensity modifications, such as contrast, blur, equalization, additive Gaussian noise, and inversions. Additionally, we implement random crops to simulate intraoperative changes to X-ray collimation or the presence of non-anatomical variations, such as surgical tools. Importantly, we do not apply any geometric image augmentations (e.g., affine warps or vertical and horizontal flips) as this would alter the ground truth pose parameters that we are attempting to regress. As a result of these heavy augmentations, our pose regression models are robust to many domain shifts that occur in intraoperative imaging and produce consistently accurate initial pose estimates.

Neural network architecture. Let \mathcal{I} represent the space of all synthetic and real X-ray images. We implement pose regression networks as $f_\theta = g \circ \mathcal{E}_\theta$, where $\mathcal{E}_\theta : \mathcal{I} \mapsto \mathbb{R}^{d+3}$ is a convolutional neural network (CNN) backbone and $g : \mathbb{R}^{d+3} \mapsto \text{SE}(3)$ is a deterministic mapping from Euclidean space to the space of all C-arm poses. The Euclidean embedding produced by the CNN represents the rotational pose parameters (\mathbb{R}^d) and the translational pose parameters (\mathbb{R}^3). As an example, for the pose parameters used to generate random poses for pretraining, $g(\alpha, \beta, \gamma, x, y, z)$ is defined as

$$\begin{bmatrix} \mathbf{R}(\alpha, \beta, \gamma) & \mathbf{R}(\alpha, \beta, \gamma)(x\hat{\mathbf{i}} + y\hat{\mathbf{j}} + z\hat{\mathbf{k}}) \\ \mathbf{0} & 1 \end{bmatrix}, \quad (25)$$

where $\mathbf{R}(\alpha, \beta, \gamma)$ is defined in Eq. (7) and the form of this random pose is given by Eq. (4). \mathcal{E}_θ is implemented using a ResNet18 [82]. All synthetic X-rays were rendered at 128×128 pixels using trilinear interpolation with a batch size of 116 X-rays per iteration. We train all patient-specific pose regression models on a single NVIDIA RTX A6000 GPU.

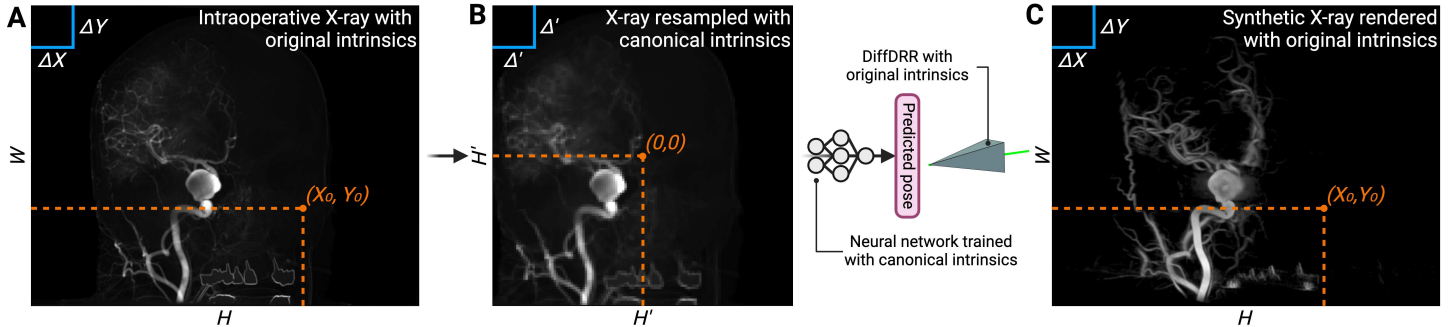


Figure S2. Making pose estimation neural networks calibration-invariant. (A) Using simple morphological operations, an intraoperative X-ray image with some set of intrinsic parameters—height H , width W , pixel spacing ($\Delta X, \Delta Y$), principal point (X_0, Y_0) , and source-to-detector distance—is resampled to the canonical intrinsics used for rendering synthetic X-rays when training the patient-specific neural network. (B) As a result, the resampled X-ray has a spatial resolution that matches the network’s training data. (C) After this network predicts the pose of the image, xvr can render the predicted X-ray with the intrinsic parameters of the original image. That is, the synthetic X-ray is rendered with the original high-resolution for pose refinement via iterative optimization.

M.4 Transfer learning. Reusing the weights of a patient-agnostic model enables ultra-fast patient-specific finetuning. However, it introduces an additional complexity: pose estimates produced by patient-agnostic models are in the reference frame of the pretraining dataset, not the preoperative volume of interest. To correct for this, we transform predicted poses from a patient-agnostic model by mapping the patient-specific preoperative volume to the registration template.

DeepFluoro. For each CT scan in the DeepFluoro dataset, we rigidly registered it to the CTPelvic1K template using ANTs [62], which requires only a few additional seconds.

Ljubljana. While TOF MRAs image the brain, which is greatly advantageous for existing 3D/3D registration methods, 3D rDSAs only contain the vasculature. This makes rigid registration of rDSAs to the pretraining dataset particularly challenging (Fig. 3B, top). Therefore, we simply center-aligned preoperative volumes to the pretraining dataset, *i.e.*, translating the volumes to register their isocenters.

Brigham. Each CT in the Brigham dataset was rigidly registered to the template TotalSegmentator scan using ANTs.

M.5 Adapting to variable intrinsic parameters (Fig. S2). Neural networks used to regress landmark locations or C-arm poses from X-rays—including our patient-specific models—are typically trained using a fixed set of intrinsic parameters (*e.g.*, source-to-detector distance, detector height and width, pixel spacing, *etc.*). However, this is incongruous with clinical workflows, as these models cannot adapt to the interventionalist changing image acquisition parameters on-the-fly (*e.g.*, panning the C-arm detector or narrowing the field of view to better visualize a particular structure). This clinical reality is not reflected in the DeepFluoro dataset as those images were collected during a cadaver study, and therefore the C-arm’s intrinsic parameters were identical for every image. However, since the DSA images in the Ljubljana dataset were collected as part of real interventions, each image acquisition has different intrinsic parameters.

To address this intraoperative challenge, we developed

a simple geometric procedure for resampling an acquired X-ray image with a given set of intrinsic parameters to a canonical set of intrinsics using only basic image processing operations (*i.e.*, translation, cropping, and bilinear interpolation) (Fig. S2, left). With these operations, we resample an intraoperative image as if it were acquired using the same canonical intrinsic parameters with which the patient’s pose regression model was trained, allowing the neural network to perform pose regression independent of changing intrinsic parameters. While intraoperative images are resampled for initial pose estimation by the neural network, we render synthetic X-rays with the original intrinsic parameters during intraoperative pose refinement (Fig. S2, right).

This approach is in contrast to training a neural network to be invariant to changes in the image acquisition, for example, by rendering synthetic X-rays with varying intrinsic parameters. We do not adopt this strategy as it requires including five additional degrees of freedom to the parameter space during simulation. As we currently randomize the six pose parameters, including additionally simulating the intrinsic parameters would dramatically increase the training time. Furthermore, ground-truth intrinsic parameters are readable from the Digital Imaging and Communications in Medicine (DICOM) header, allowing us to directly utilize known geometric information rather than training a model to recapitulate *a priori* recorded measurements.

M.6 Pose refinement (Fig. S3). While neural networks in xvr typically produce pose estimates within 20 mm to 30 mm of the ground truth pose, this error is not uniform across all the degrees of freedom that constitute the C-arm’s pose. In Fig. S3A, left, we visualize the distribution of error per degree of freedom in initial pose estimates (the geometric meaning of each parameter is illustrated in Fig. 1C). While the rotational degrees of freedom each have roughly $\pm 2.5^\circ$ of initial misestimation error (Fig. S3A, top left), the translational degrees of freedom display much greater heterogeneity. For example, the in-plane translations (x and z) incur errors of only ± 1.5 mm, but the source-to-isocenter distance (y) incurs errors of ± 15 mm (Fig. S3A, bottom left). This is because

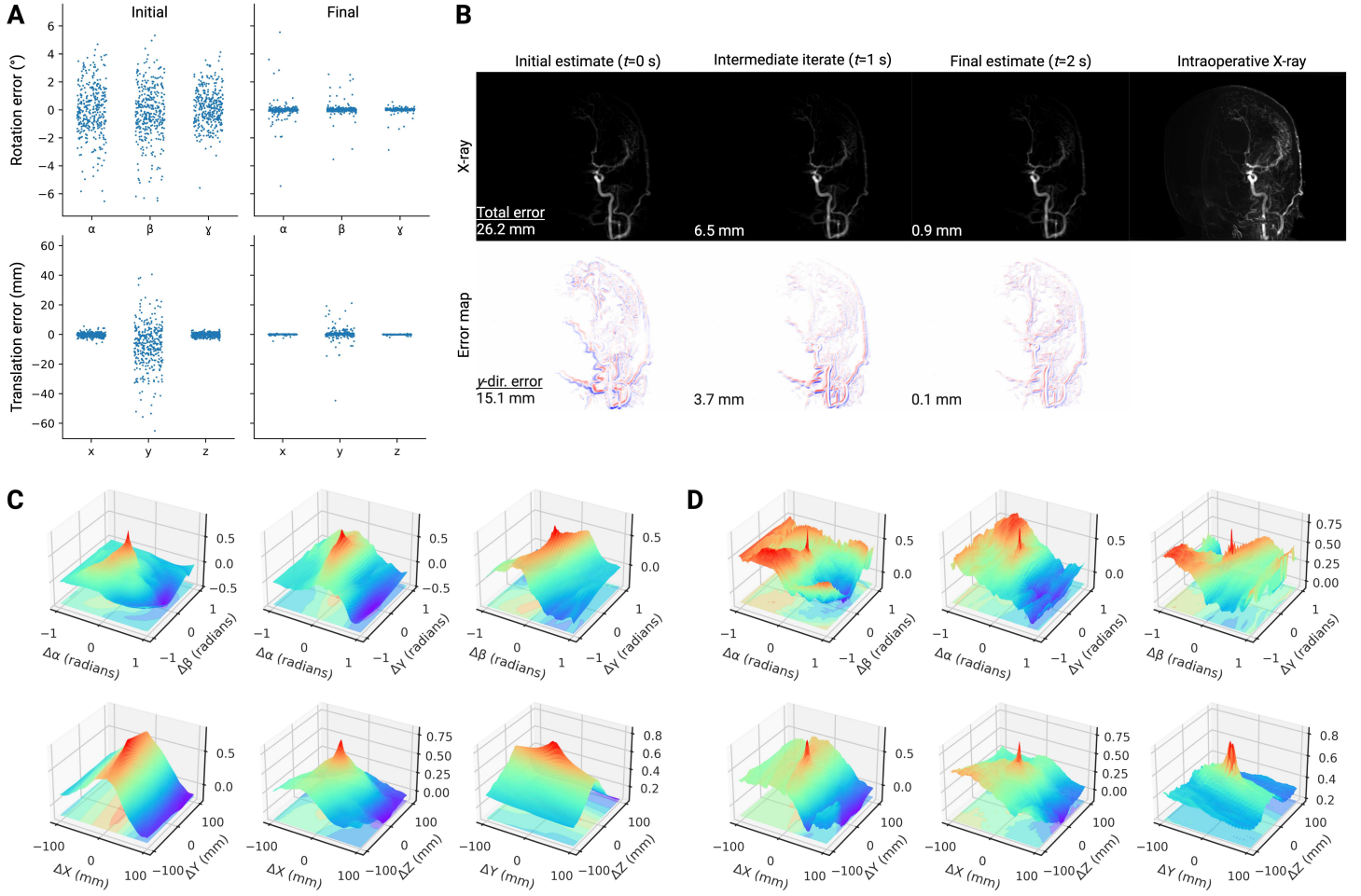


Figure S3. Intraoperative pose refinement strategy. **(A)** Estimation errors of the six pose parameters before (*left*) and after *right* iterative optimization. All rotational parameters incur roughly $\pm 2.5^\circ$ of error and in-plane translational parameters (x and z) incur roughly ± 1.5 mm of error. However, the source-to-isocenter distance (y) incurs errors of ± 15 mm, demonstrating the neural network's difficulty in accurately estimating depth. **(B)** Intraoperative pose refinement takes about 2 s and successfully overcomes the depth error in the network's initial pose estimate. **(C)** The loss landscape induced by multiscale normalized cross correlation (mNCC) is smooth in a large neighborhood around the true pose, broadening the capture radius of our pose refinement strategy. However, mNCC is relatively non-specific about the true pose. **(D)** In contrast, the loss landscape induced by gradient normalized cross correlation (gNCC) results in a more specific optimum at the expense of a rougher landscape further from the true pose. Averaging mNCC and gNCC enables *xvr* to achieve submillimeter accurate pose refinement.

the resulting X-ray image changes very subtly for even large changes in the distance from the X-ray source to the object. To illustrate this phenomenon, we show an example of the iterative optimization process in Fig. S3B. While the different iterates do not appear particularly visually distinct, the registration error decreases from 26.2 mm to 0.9 mm after iterative optimization (Fig. S3B, *top*). In particular, the error of the estimated source-to-isocenter distance reduces from 15.1 mm to 0.1 mm (Fig. S3B, *bottom*). Furthermore, this example highlights the inherent difficulty of attempting to perform manual 2D/3D registration, as all the synthetic X-rays appear very visually similar to the intraoperative X-ray despite having wildly different pose estimation accuracy.

Image similarity metric. With the goal of achieving submillimeter registration accuracy, we tested multiple image similarity metrics to determine which enables the precise recovery of the true values of all pose parameters. The first

metric we considered was multiscale normalized cross correlation (mNCC) [53], which has previously been shown to increase the capture radius of 2D/3D registration via iterative optimization [53]. Second, we considered gradient normalized cross correlation (gradNCC) [70], an image similarity metric that computes the correlation between Sobel-filtered versions of the two images. As this metric encourages the alignment of the edges in the two images, it is better suited for depth estimation than mNCC [54].

To evaluate the behavior of these image similarity metrics, we visualize their loss landscapes (Fig. S3C and D). To do so, we render synthetic X-rays at perturbations from the ground truth pose ($\pm 60^\circ$ for rotational parameters and 100 mm for translational parameters) and measure their similarity to the intraoperative X-ray. The loss landscape for mNCC is very smooth in this large region around the ground truth pose, which means that it is an ideal objective function to optimize

when the initial pose estimate has high error (Fig. S3C). However, this visualization also shows that the gradients of mNCC in the y -direction are relatively small. Whereas each of the other pose parameters has well-defined peaks, which lead to more precise and efficient optimization, the loss landscape of mNCC in the y -direction is relatively saddle-like, suggesting that pose refinement with mNCC may misestimate the source-to-isocenter distance of an intraoperative X-ray by a few millimeters. In contrast, gradNCC has a much sharper landscape about the true source-to-isocenter distance (Fig. S3D). However, unlike mNCC, gradNCC is much less smooth far away from the ground truth pose and is therefore less robust to poor initial pose estimates. Therefore, to combine the advantages of both metrics, we perform pose refinement by optimizing the average of mNCC and gradNCC, enabling robust and precise submillimeter-accurate 2D/3D registration (Fig. 4).

Structure-specific registration. If a segmentation map is available for the preoperative volume (e.g., from TotalSegmentator [69]), we can use the ability of our renderer to generate X-ray images of specific parts of the preoperative volume to register individual anatomical structures. Specifically, for pelvic registration, we only render the left and right hips, sacrum, and L5 vertebra. By modeling those objects as a single rigid object, we enable our registration framework to be invariant to irrelevant domain shifts, such as the motion of the femur between the preoperative and intraoperative imaging. While segmentation labels are relatively easy to derive for most structures on CT and MRI thanks to open-source tools such as TotalSegmentator [69], other structures like vessels remain difficult to segment. Therefore, we note that for neurovascular registration, we do not use segmentation labels to guide registration. Despite this, we still achieve submillimeter-accurate results.

Multiscale registration. To improve intraoperative registration speeds, we implement a multiscale rendering protocol that registers X-ray images at progressively higher resolutions. Specifically, when optimization of the image similarity metric plateaus at a particular scale, we progress to the next higher resolution. This coarse-to-fine registration strategy enables simultaneous optimization of global anatomical misalignment and local refinement of fine structures.

M.7 Parsing pose parameters from DICOM headers. Imaging data stored as DICOM files contain additional metadata beyond the raw pixel intensities of the image. In particular, X-ray angiography DICOM files encode the primary and secondary positioner angles of the C-arm, which correspond to the rotational parameters α and β , and the Source to Patient Distance attribute, which represents the y -direction translation (Fig. 1C). Note that these comprise only three of the six degrees of freedom required to describe a C-arm pose as formulated in Eq. (25). Furthermore, while this partially specifies the pose of the C-arm, this formulation does not account for *the position of the patient relative to the C-arm*. That is, unless the isocenter of the patient’s CT is perfectly aligned at the C-arm’s center of rotation, this pose will have misidentified translations.

References

[1] Mahadevappa Mahesh, Armin J Ansari, and Fred A Mettler Jr. Patient exposure from radiologic and nuclear medicine procedures in the united states and worldwide: 2009–2018. *Radiology*, 307(1):e221263, 2022.

[2] Chris Schulz, Stephan Waldeck, and Uwe Max Mauer. Intraoperative image guidance in neurosurgery: development, current indications, and future trends. *Radiology research and practice*, 2012(1):197364, 2012.

[3] Matthew A Kirkman. The role of imaging in the development of neurosurgery. *Journal of Clinical Neuroscience*, 22(1):55–61, 2015.

[4] R Phillips, WJ Viant, AMMA Mohsen, JG Griffiths, MA Bell, TJ Cain, KP Sherman, and MRK Karpinski. Image guided orthopaedic surgery design and analysis. *Transactions of the Institute of Measurement and Control*, 17(5):251–264, 1995.

[5] Terry M Peters. Image-guided surgery: from x-rays to virtual reality. *Computer methods in biomechanics and biomedical engineering*, 4(1):27–57, 2001.

[6] Stephen Rudin, Daniel R Bednarek, and Kenneth R Hoffmann. Endovascular image-guided interventions (eigis). *Medical physics*, 35(1):301–309, 2008.

[7] Vania Tacher, MingDe Lin, Pascal Desgranges, Jean-Francois Deux, Thijs Grünhagen, Jean-Pierre Becquemin, Alain Luciani, Alain Rahmouni, and Hicham Kobeiter. Image guidance for endovascular repair of complex aortic aneurysms: comparison of two-dimensional and three-dimensional angiography and image fusion. *Journal of Vascular and Interventional Radiology*, 24(11):1698–1706, 2013.

[8] Catherine A McBain, Ann M Henry, Jonathan Sykes, Ali Amer, Tom Marchant, Christopher M Moore, Julie Davies, Julia Stratford, Claire McCarthy, Bridget Portritt, et al. X-ray volumetric imaging in image-guided radiotherapy: the new standard in on-treatment imaging. *International Journal of Radiation Oncology* Biology* Physics*, 64(2):625–634, 2006.

[9] Laura A Dawson and David A Jaffray. Advances in image-guided radiation therapy. *Journal of clinical oncology*, 25(8):938–946, 2007.

[10] Florian Sterzing, Rita Engenhart-Cabillic, Michael Flenchte, and Jürgen Debus. Image-guided radiotherapy: a new dimension in radiation oncology. *Deutsches Aerzteblatt International*, 108(16):274, 2011.

[11] Shaheen E Lakhani, Anna Kaplan, Cyndi Laird, and Yaakov Leiter. The interventionalism of medicine: interventional radiology, cardiology, and neuroradiology. *International archives of medicine*, 2(1):27, 2009.

[12] Thomas J Vogl, Wolfgang Reith, and Ernst J Rummey. *Diagnostic and interventional radiology*. Springer, 2016.

[13] Kristy K Brock, Stephen R Chen, Rahul A Sheth, and Jeffrey H Siewersden. Imaging in interventional radiology: 2043 and beyond. *Radiology*, 308(1):e230146, 2023.

[14] E Vano, R Sanchez, JM Fernandez, F Rosales, MA Garcia, J Sotil, J Hernandez, F Carrera, J Ciudad, MM Soler, et al. Importance of dose settings in the x-ray systems used for interventional radiology: a national survey. *Cardiovascular and interventional radiology*, 32:121–126, 2009.

[15] Raj R Makkar, Vinod H Thourani, Michael J Mack, Susheel K Kodali, Samir Kapadia, John G Webb, Sung-Han Yoon, Alfredo Trento, Lars G Svensson, Howard C Herrmann, et al. Five-year outcomes of transcatheter or surgical aortic-valve replacement. *New England Journal of Medicine*, 382(9):799–809, 2020.

[16] RM Greenhalgh. Comparison of endovascular aneurysm repair with open repair in patients with abdominal aortic aneurysm (evar trial 1), 30-day operative mortality results: randomised controlled trial. *The Lancet*, 364(9437):843–848, 2004.

[17] Francois H Cornelis, Omar Dzaye, Helmut Schoellnast, and Stephen B Solomon. Imaging of interventional therapies in oncology: Image guidance, robotics, and fusion systems. *Interventional Oncology: A Multidisciplinary Approach to Image-Guided Cancer Therapy*, pages 1–17, 2023.

[18] Balraj S Jhawar, Demytra Mitsis, and Neil Duggal. Wrong-sided and wrong-level neurosurgery: a national survey. *Journal of Neurosurgery: Spine*, 7(5):467–472, 2007.

[19] Milan G Mody, Ali Nourbakhsh, Daniel L Stahl, Mark Gibbs, Mohammad Alfawareh, and Kim J Garges. The prevalence of wrong level surgery among spine surgeons. *Spine*, 33(2):194–198, 2008.

[20] Krishna Kandarpa and Lindsay Machan. *Handbook of interventional radiologic procedures*. Lippincott Williams & Wilkins, 2011.

[21] Jérôme Tonetti, Mehdi Boudissa, Gael Kerschbaumer, and Olivier Seurat. Role of 3d intraoperative imaging in orthopedic and trauma surgery. *Orthopaedics & Traumatology: Surgery & Research*, 106(1):S19–S25, 2020.

[22] Andrew Abumoussa, Vivek Gopalakrishnan, Benjamin Succop, Michael Galgano, Sivakumar Jaikumar, Yueh Z Lee, and Deb A Bhowmick. Machine learning for automated and real-time two-dimensional to three-dimensional registration of the spine using a single radiograph. *Neurosurgical Focus*, 54(6):E16, 2023.

[23] Pieter Maria Mielekamp and Nicolaas Jan Noordhoek. Method and device for displaying a first image and a second image of an object, March 6 2018. US Patent 9,910,958.

[24] Roshan Ramakrishna Naik, Anitha Hoblidar, Shyam Sunder N Bhat, Nishanth Ampar, and Raghuraj Kundanagar. A hybrid 3d-2d image registration framework for pedicle screw trajectory registration between intraoperative x-ray image and preoperative ct image. *Journal of Imaging*, 8(7):185, 2022.

[25] Coert T Metz, Michiel Schaap, Stefan Klein, Lisan A Neefjes, Ermanno Capuano, Carl Schultz, Robert Jan Van Geuns, Patrick W Serruys, Theo Van Walsum, and Wiro J Niessen. Patient specific 4d coronary models from ecg-gated cta data for intra-operative dynamic alignment of cta with x-ray images. In *Medical Im-*

age Computing and Computer-Assisted Intervention—*MICCAI 2009: 12th International Conference, London, UK, September 20-24, 2009, Proceedings, Part I* 12, pages 369–376. Springer, 2009.

[26] André Aichert, Martin Berger, Jian Wang, Nicole Maass, Arnd Doerfler, Joachim Hornegger, and Andreas K Maier. Epipolar consistency in transmission imaging. *IEEE transactions on medical imaging*, 34(11):2205–2219, 2015.

[27] Martin Wagner, Sebastian Schafer, Charles Strother, and Charles Mistretta. 4d interventional device reconstruction from biplane fluoroscopy. *Medical physics*, 43(3):1324–1334, 2016.

[28] Marc L Kessler. Image registration and data fusion in radiation therapy. *The British Institute of Radiology*, 79: S99–S108, 2006.

[29] Elizabeth Huynh, Ahmed Hosny, Christian Guthier, Danielle S Bitterman, Steven F Petit, Daphne A Haas-Kogan, Benjamin Kann, Hugo JW Aerts, and Raymond H Mak. Artificial intelligence in radiation oncology. *Nature Reviews Clinical Oncology*, 17(12):771–781, 2020.

[30] Krish Bhadra, Otis B Rickman, Amit K Mahajan, and Douglas Kyle Hogarth. A robotic electromagnetic navigation bronchoscopy with integrated tool-in-lesion-tomosynthesis technology: The MATCH study. *Journal of Bronchology & Interventional Pulmonology*, 31(1): 23–29, 2024.

[31] Yoonho Kim, Emily Genevriere, Pablo Harker, Jaehun Choe, Marcin Balicki, Robert W Regenhardt, Justin E Vranic, Adam A Dmytriw, Aman B Patel, and Xuanhe Zhao. Telerobotic neurovascular interventions with magnetic manipulation. *Science Robotics*, 7(65):eabg9907, 2022.

[32] Mathias Unberath, Cong Gao, Yicheng Hu, Max Judish, Russell H Taylor, Mehran Armand, and Robert Grupp. The impact of machine learning on 2D/3D registration for image-guided interventions: A systematic review and perspective. *Frontiers in Robotics and AI*, 8:716007, 2021.

[33] S Ébastien Clippe, David Sarrut, Claude Malet, Serge Miguët, Chantal Ginestet, and Christian Carrie. Patient setup error measurement using 3d intensity-based image registration techniques. *International Journal of Radiation Oncology* Biology* Physics*, 56(1):259–265, 2003.

[34] L Lemieux, R Jagoe, DR Fish, ND Kitchen, and DGT Thomas. A patient-to-computed-tomography image registration method based on digitally reconstructed radio-graphs. *Medical physics*, 21(11):1749–1760, 1994.

[35] Graeme P Penney, Jürgen Weese, John A Little, Paul Desmedt, Derek LG Hill, et al. A comparison of similarity measures for use in 2-d-3-d medical image registration. *IEEE transactions on medical imaging*, 17(4):586–595, 1998.

[36] Dotan Knaan and Leo Joskowicz. Effective intensity-based 2d/3d rigid registration between fluoroscopic x-ray and ct. In *International Conference on Medical Image Computing and Computer-Assisted Intervention*, pages 351–358. Springer, 2003.

[37] L Zollei, Eric Grimson, Alexander Norbush, and W Wells. 2d-3d rigid registration of x-ray fluoroscopy and ct images using mutual information and sparsely sampled histogram estimators. In *Proceedings of the 2001 IEEE Computer Society Conference on Computer Vision and Pattern Recognition. CVPR 2001*, volume 2, pages II–II. IEEE, 2001.

[38] Vivek Gopalakrishnan and Polina Golland. Fast auto-differentiable digitally reconstructed radiographs for solving inverse problems in intraoperative imaging. In *Workshop on Clinical Image-Based Procedures*, pages 1–11. Springer, 2022.

[39] Mohamed R Mahfouz, William A Hoff, Richard D Komiscek, and Douglas A Dennis. A robust method for registration of three-dimensional knee implant models to two-dimensional fluoroscopy images. *IEEE transactions on medical imaging*, 22(12):1561–1574, 2003.

[40] B-M You, Pepe Siy, William Anderst, and Scott Tashman. In vivo measurement of 3-d skeletal kinematics from sequences of biplane radiographs: application to knee kinematics. *IEEE transactions on medical imaging*, 20(6):514–525, 2001.

[41] Cong Gao, Xingtong Liu, Wenhao Gu, Benjamin Killeen, Mehran Armand, Russell Taylor, and Mathias Unberath. Generalizing spatial transformers to projective geometry with applications to 2d/3d registration. In *Medical Image Computing and Computer Assisted Intervention—MICCAI 2020: 23rd International Conference, Lima, Peru, October 4–8, 2020, Proceedings, Part III* 23, pages 329–339. Springer, 2020.

[42] Wenhao Gu, Cong Gao, Robert Grupp, Javad Fotouhi, and Mathias Unberath. Extended capture range of rigid 2d/3d registration by estimating riemannian pose gradients. In *Machine Learning in Medical Imaging: 11th International Workshop, MLMI 2020, Held in Conjunction with MICCAI 2020, Lima, Peru, October 4, 2020, Proceedings* 11, pages 281–291. Springer, 2020.

[43] Cong Gao, Anqi Feng, Xingtong Liu, Russell H Taylor, Mehran Armand, and Mathias Unberath. A fully differentiable framework for 2d/3d registration and the projective spatial transformers. *IEEE transactions on medical imaging*, 2023.

[44] Primoz Markelj, Dejan Tomažević, Bostjan Likar, and Franjo Pernuš. A review of 3d/2d registration methods for image-guided interventions. *Medical image analysis*, 16(3):642–661, 2012.

[45] Robert B Grupp, Rachel A Hegeman, Ryan J Murphy, Clayton P Alexander, Yoshito Otake, Benjamin A McArthur, Mehran Armand, and Russell H Taylor. Pose estimation of periacetabular osteotomy fragments with intraoperative x-ray navigation. *IEEE transactions on biomedical engineering*, 67(2):441–452, 2019.

[46] Bastian Bier, Florian Goldmann, Jan-Nico Zaech, Javad Fotouhi, Rachel Hegeman, Robert Grupp, Mehran Armand, Greg Osgood, Nassir Navab, Andreas Maier, et al. Learning to detect anatomical landmarks of the

pelvis in x-rays from arbitrary views. *International journal of computer assisted radiology and surgery*, 14:1463–1473, 2019.

[47] Javier Esteban, Matthias Grimm, Mathias Unberath, Guillaume Zahnd, and Nassir Navab. Towards fully automatic x-ray to ct registration. In *Medical Image Computing and Computer Assisted Intervention–MICCAI 2019: 22nd International Conference, Shenzhen, China, October 13–17, 2019, Proceedings, Part VI 22*, pages 631–639. Springer, 2019.

[48] Pragyan Shrestha, Chun Xie, Hidehiko Shishido, Yuichi Yoshii, and Itaru Kitahara. X-ray to ct rigid registration using scene coordinate regression. In *International Conference on Medical Image Computing and Computer-Assisted Intervention*, pages 781–790. Springer, 2023.

[49] Pragyan Shrestha, Chun Xie, Yuichi Yoshii, and Itaru Kitahara. Rayemb: Arbitrary landmark detection in x-ray images using ray embedding subspace. *arXiv preprint arXiv:2410.08152*, 2024.

[50] Shun Miao, Z Jane Wang, and Rui Liao. A cnn regression approach for real-time 2d/3d registration. *IEEE transactions on medical imaging*, 35(5):1352–1363, 2016.

[51] Mai Bui, Shadi Albarqouni, Michael Schrapp, Nassir Navab, and Slobodan Ilic. X-ray posenet: 6 dof pose estimation for mobile x-ray devices. In *2017 IEEE Winter Conference on Applications of Computer Vision (WACV)*, pages 1036–1044. IEEE, 2017.

[52] Baochang Zhang, Shahrooz Faghihroohi, Mohammad Farid Azampour, Shuting Liu, Reza Ghotbi, Heribert Schunkert, and Nassir Navab. A patient-specific self-supervised model for automatic x-ray/ct registration. In *International Conference on Medical Image Computing and Computer-Assisted Intervention*, pages 515–524. Springer, 2023.

[53] Vivek Gopalakrishnan, Neel Dey, and Polina Golland. Intraoperative 2D/3D image registration via differentiable X-ray rendering. *arXiv preprint arXiv:2312.06358*, 2023.

[54] Robert B Grupp, Mathias Unberath, Cong Gao, Rachel A Hegeman, Ryan J Murphy, Clayton P Alexander, Yoshito Otake, Benjamin A McArthur, Mehran Armand, and Russell H Taylor. Automatic annotation of hip anatomy in fluoroscopy for robust and efficient 2D/3D registration. *International journal of computer assisted radiology and surgery*, 15:759–769, 2020.

[55] Cong Gao, Benjamin D Killeen, Yicheng Hu, Robert B Grupp, Russell H Taylor, Mehran Armand, and Mathias Unberath. Synthetic data accelerates the development of generalizable learning-based algorithms for x-ray image analysis. *Nature Machine Intelligence*, 5(3):294–308, 2023.

[56] Robert L Siddon. Fast calculation of the exact radiological path for a three-dimensional CT array. *Medical physics*, 12(2):252–255, 1985.

[57] Pranav Rajpurkar, Emma Chen, Oishi Banerjee, and Eric J Topol. AI in health and medicine. *Nature Medicine*, 28(1):31–38, 2022.

[58] Chris Varghese, Ewen M Harrison, Greg O’Grady, and Eric J Topol. Artificial intelligence in surgery. *Nature Medicine*, pages 1–12, 2024.

[59] Michael Yip, Septimiu Salcudean, Ken Goldberg, Kaspar Althoefer, Arianna Menciassi, Justin D Opfermann, Axel Krieger, Krithika Swaminathan, Conor J Walsh, He Huang, et al. Artificial intelligence meets medical robotics. *Science*, 381(6654):141–146, 2023.

[60] Uroš Mitrović, Žiga Špiclin, Boštjan Likar, and Franjo Pernuš. 3D-2D registration of cerebral angiograms: A method and evaluation on clinical images. *IEEE transactions on medical imaging*, 32(8):1550–1563, 2013.

[61] Pengbo Liu, Hu Han, Yuanqi Du, Heqin Zhu, Yinhao Li, Feng Gu, Honghu Xiao, Jun Li, Chunpeng Zhao, Li Xiao, et al. Deep learning to segment pelvic bones: large-scale CT datasets and baseline models. *International Journal of Computer Assisted Radiology and Surgery*, 16:749–756, 2021.

[62] Nicholas J Tustison, Philip A Cook, Andrew J Holbrook, Hans J Johnson, John Muschelli, Gabriel A Devenyi, Jeffrey T Duda, Sandhitsu R Das, Nicholas C Cullen, Daniel L Gillen, et al. The ANTsX ecosystem for quantitative biological and medical imaging. *Scientific reports*, 11(1):9068, 2021.

[63] NeuroImaging Tools & Resources Collaboratory. Magnetic resonance angiography atlas dataset, 2017. URL <https://www.nitrc.org/projects/icbmra/>.

[64] Marshall Xu, Fernanda L Ribeiro, Markus Barth, Michaël Bernier, Steffen Bollmann, Soumick Chatterjee, Francesco Cognolato, Omer Faruk Gulban, Vaibhavi Itkylal, Siyu Liu, et al. VesselBoost: A Python toolbox for small blood vessel segmentation in human magnetic resonance angiography data. *bioRxiv*, pages 2024–05, 2024.

[65] Diederik P Kingma. Adam: A method for stochastic optimization. *arXiv preprint arXiv:1412.6980*, 2014.

[66] Olaf Ronneberger, Philipp Fischer, and Thomas Brox. U-net: Convolutional networks for biomedical image segmentation. In *Medical image computing and computer-assisted intervention–MICCAI 2015: 18th international conference, Munich, Germany, October 5–9, 2015, proceedings, part III 18*, pages 234–241. Springer, 2015.

[67] Shiqi Li, Chi Xu, and Ming Xie. A robust O(n) solution to the Perspective-n-Point problem. *IEEE transactions on pattern analysis and machine intelligence*, 34(7):1444–1450, 2012.

[68] Michael Potente and Taija Mäkinen. Vascular heterogeneity and specialization in development and disease. *Nature Reviews Molecular Cell Biology*, 18(8):477–494, 2017.

[69] Jakob Wasserthal, Hanns-Christian Breit, Manfred T Meyer, Maurice Pradella, Daniel Hinck, Alexander W Sauter, Tobias Heye, Daniel T Boll, Joshy Cyriac, Shan Yang, et al. TotalSegmentator: robust segmentation of 104 anatomic structures in CT images. *Radiology: Artificial Intelligence*, 5(5), 2023.

[70] Robert B Grupp, Mehran Armand, and Russell H Taylor. Patch-based image similarity for intraoperative 2d/3d pelvis registration during periacetabular osteotomy. In

OR 2.0 Context-Aware Operating Theaters, Computer Assisted Robotic Endoscopy, Clinical Image-Based Procedures, and Skin Image Analysis: First International Workshop, OR 2.0 2018, 5th International Workshop, CARE 2018, 7th International Workshop, CLIP 2018, Third International Workshop, ISIC 2018, Held in Conjunction with MICCAI 2018, Granada, Spain, September 16 and 20, 2018, Proceedings 5, pages 153–163. Springer, 2018.

[71] Rohit Jena, Deeksha Sethi, Pratik Chaudhari, and James Gee. Deep learning in medical image registration: Magic or mirage? In *The Thirty-eighth Annual Conference on Neural Information Processing Systems*, 2024. URL <https://openreview.net/forum?id=lZJ0WYI5YC>.

[72] Hanna Siebert, Christoph Großbröhmer, Lasse Hansen, and Mattias P Heinrich. Convexadam: Self-configuring dual-optimisation-based 3d multitask medical image registration. *IEEE Transactions on Medical Imaging*, 2024.

[73] Neel Dey, Benjamin Billot, Hallee E. Wong, Clinton Wang, Mengwei Ren, Ellen Grant, Adrian V Dalca, and Polina Golland. Learning general-purpose biomedical volume representations using randomized synthesis. In *The Thirteenth International Conference on Learning Representations*, 2025. URL <https://openreview.net/forum?id=x0mC5LiVuN>.

[74] Borjan Gagoski, Junshen Xu, Paul Wighton, M Dylan Tisdall, Robert Frost, Wei-Ching Lo, Polina Golland, Andre van Der Kouwe, Elfar Adalsteinsson, and P Ellen Grant. Automated detection and reacquisition of motion-degraded images in fetal HASTE imaging at 3 T. *Magnetic resonance in medicine*, 87(4):1914–1922, 2022.

[75] Saugat Kandel, Tao Zhou, Anakha V Babu, Zichao Di, Xinxin Li, Xuedan Ma, Martin Holt, Antonino Miceli, Charudatta Phatak, and Mathew J Cherukara. Demonstration of an ai-driven workflow for autonomous high-resolution scanning microscopy. *Nature Communications*, 14(1):5501, 2023.

[76] Chelsea Finn, Pieter Abbeel, and Sergey Levine. Model-agnostic meta-learning for fast adaptation of deep networks. In *International conference on machine learning*, pages 1126–1135. PMLR, 2017.

[77] Shaojie Bai, J Zico Kolter, and Vladlen Koltun. Deep equilibrium models. *Advances in neural information processing systems*, 32, 2019.

[78] Rohit Jena, Pratik Chaudhari, and James C Gee. Deep implicit optimization for robust and flexible image registration. *arXiv preprint arXiv:2406.07361*, 2024.

[79] Adam Paszke, Sam Gross, Francisco Massa, Adam Lerer, James Bradbury, Gregory Chanan, Trevor Killeen, Zeming Lin, Natalia Gimelshein, Luca Antiga, et al. Pytorch: An imperative style, high-performance deep learning library. *Advances in neural information processing systems*, 32, 2019.

[80] Richard Hartley and Andrew Zisserman. *Multiple view geometry in computer vision*. Cambridge university press, 2003.

[81] Mohammadhossein Momeni, Vivek Gopalakrishnan, Neel Dey, Polina Golland, and Sarah Frisken. Differentiable voxel-based X-ray rendering improves sparse-view 3D CBCT reconstruction, 2024. URL <https://arxiv.org/abs/2411.19224>.

[82] Kaiming He, Xiangyu Zhang, Shaoqing Ren, and Jian Sun. Deep residual learning for image recognition. In *Proceedings of the IEEE conference on computer vision and pattern recognition*, pages 770–778, 2016.